

Light propagation in two-dimensional and three-dimensional slabs of reflective colloidal particles in solution: The effect of interfaces and interparticle correlations

Raffaella Cabriolu,^{1,*} Sarah Dungan,² and Pietro Ballone^{2,3}

¹*Department of Physics, Norwegian University of Science and Technology (NTNU), 7491 Trondheim, Norway*

²*School of Physics, University College Dublin, Dublin 4, Ireland*

³*Conway Institute for Biomolecular and Biomedical Research, University College Dublin, Dublin 4, Ireland*



(Received 8 July 2023; accepted 21 December 2023; published 23 January 2024)

The propagation of light across 2D and 3D slabs of reflective colloidal particles in a fluidlike state has been investigated by simulation. The colloids are represented as hard spheres with and without an attractive square-well tail. Representative configurations of particles have been generated by Monte Carlo. The path of rays entering the slab normal to its planar surface has been determined by exact geometric scattering conditions, assuming that particles are macroscopic spheres fully reflective at the surface of their hard-core potential. The analysis of light paths provides the transmission and reflection coefficients, the mean-free path, the average length of transmitted and reflected paths, the distribution of scattering events across the slab, the angular spread of the outgoing rays as a function of dimensionality, and thermodynamic state. The results highlight the presence of a sizable population of very long paths, which play an important role in random lasing from solutions of metal particles in an optically active fluid. The output power spectrum resulting from the stimulated emission amplification decays asymptotically as an inverse power law. The present study goes beyond the standard approach based on a random walk confined between two planar interfaces and parametrized in terms of the mean-free path and scattering matrix. Here, instead, the mean-free path, the correlation among scattering events, and memory effects are not assumed *a priori*, but emerge from the underlying statistical mechanics model of interacting particles. In this way the dependence of properties on the thermodynamic state, the effect of particle-particle and particle-interface correlations and of spatial inhomogeneity, and memory effects are accounted for in a transparent way. Moreover, the approach joins smoothly the ballistic regime of light propagation at low density with the diffusive regime at high density of scattering centers. These properties are exploited to investigate the effect of weak polydispersivity and of large density fluctuations at the critical point of the model with the attractive potential tail.

DOI: [10.1103/PhysRevE.109.014615](https://doi.org/10.1103/PhysRevE.109.014615)

I. INTRODUCTION

The scattering of light in disordered media is a subject of great conceptual and practical interest, which underlies natural phenomena such as the rainbow [1] and the metallic hues of selected butterflies and beetles, as well as the iridescent glazing of ancient Chinese pottery. The interest in this subject has been renewed and enhanced by its applications in photonics and nanophotonics in particular.

One specific case of application is represented by random lasing. Conventional lasers [2] rely on the amplification of light by stimulated emission in an active medium whose population inversion is driven by a secondary light source. Their gain is typically due to the coupling to a high-quality optical cavity, whose mode selectivity and sizable energy density are instrumental in achieving strong beam intensity, coherence, and collimation. High amplification of light, however, does not strictly require a highly tuned optical cavity [3,4], since it can be achieved also using simpler setups such as the variety of devices known as random lasers (RLs) [5,6]. In these systems, amplification relies on the propagation through an optically active medium of a beam of light whose path is

lengthened by multiple reflections from a static or dynamic disordered distribution of scattering centers. The appeal of random lasers is due, first of all, to the simplicity of their fabrication, since these systems are largely self-assembled. To a lesser extent, it is also due to the contrast of structural randomness and cooperative optical emission. Depending on the type and structure of the underlying medium, on the feedback mechanism, and on the light intensity, the output of RLs can be coherent [7] or, more often, incoherent light [8]. Even random lasers can support discrete modes, but often, especially in the incoherent feedback case, the emission spectrum is rather broad, and directionality is lacking. Both features could represent advantages or disadvantages depending on the application.

Arguably, the simplest realization of RLs is represented by particles of μm to mm diameter dispersed at equilibrium conditions (colloids) [9], or out of equilibrium (shaken granular systems) [10,11] in an optically active fluid. A paradigmatic case is represented by μm TiO_2 colloidal particles dissolved in a solution of fluorescent organic molecules [9]. Then the scattering of light is due to the difference of refraction index between particles and the solution, while the amplification is due to the optical pumping of the organic dye. Other dielectric oxides (ZnO , Al_2O_3 , etc.) and metal particles are used as well.

*raffaella.cabriolu@ntnu.no

From the conceptual point of view, random lasers are at the crossroad of several different research topics. First of all, the propagation of wavelike excitations in a medium sprinkled by a disordered distribution of scattering centers is a central theme of statistical mechanics [12,13], with implications for a broad range of subjects, exemplified by the propagation of light in glasses and defective crystals [14] and of electrons in disordered metal alloys [15–17], the localization of vibrations in amorphous materials [18], the scattering of light from aerosols in the atmosphere [19], and the diffusion of cold atoms in disordered lattices [20]. Despite lacking some of the characteristic features of conventional lasers, random lasers as well find application in a number of different fields, such as photonics [21], display technology, sensing, speckle-free imaging [22], and light therapy while further applications are under development in diagnostics exploiting the random lasing in human tissues infiltrated with an organic dye solution [23]. New conceptual developments and the introduction of new materials [24] can still greatly extend the application range of RLs.

Because of their broad interest, RLs have been extensively investigated by theoretical methods [25–31] and by simulation [19,32–35], accounting for a variety of aspects in the nature of the scattering centers and of the scattering process (Mie scattering, reflective hard spheres for colloids, etc.), including the competition and sometimes the interference of different wave beams propagating in the medium. In the simplest case of colloids in an optically active solvent, and with RLs based on granular matter, theoretical and computational studies are focused primarily on systems with a high density of scattering centers, in which the propagation of light is diffusive. In this regime the underlying kinetics of light has been, in most cases, modeled as a random walk in a finite slab, with preassigned distribution of scattering probability. More first-principle approaches to account for correlation among scattering events have been proposed (see, for instance, Ref. [36]) but rarely applied. The idealized random walk approaches, however, require additional parameters and *ad hoc* assumptions to model changes in the thermodynamic conditions and in the interparticle potential, or the effect of inhomogeneities in the system. Thus, these parametrized models might not reproduce exactly all the correlations found in real colloidal systems, nor account consistently for density oscillations at surfaces and interfaces or for large-scale inhomogeneities in samples approaching criticality.

To cover also these phenomena, we model the scattering of a light beam from a collection of hard spheres with and without an attractive tail, floating into a fluid environment, represented as a slab confined by two planar, parallel surfaces. The model closely corresponds to macroscopic dielectric [37,38] or metal particles [7,39] in a finite container, which could represent the core of a random laser.

Particle configurations are generated by Monte Carlo simulation, hence they fully account for the exact correlations in the positions of scattering centers, and also they contain exactly the effect of interfaces and of density fluctuations at all wavelengths.

The purpose of our study is to investigate the effects of the packing fraction of colloidal particles on various properties of the light incident on the system, including the path length, the

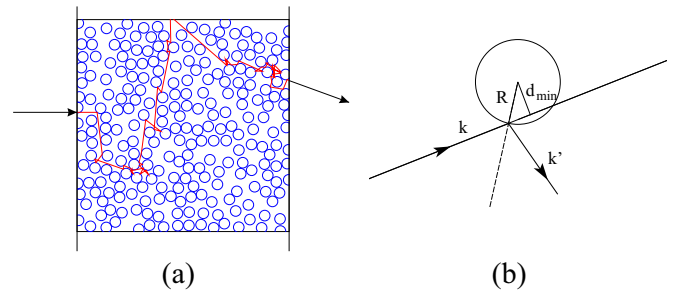


FIG. 1. Schematic representation of the computational set up in two dimensions.

amplification of the input light, the coefficients of transmission and reflection, the density distribution of scattering events along the axis orthogonal to the slab, and the angular distribution of the output light. The geometric optics framework underlying the present study neglects wave interference and diffraction, as well as any nonlinearity, due, for instance, to the depletion of excited states at high beam intensity. Our model, therefore, describes intensity feedback, which is also incoherent. On the other hand, the exact application of the geometric optics relations allows one to match smoothly the ballistic regime of light propagation at low density of the scattering spheres with the diffusive regime at high density. In a different but related context, the model and its results might be of interest in the analysis of reflectance and transmission of light from a turbid medium [13,40–42].

II. MODEL AND METHOD

The present computational investigation has been inspired by the experimental study in Ref. [10], whose setup consists of $\sim 10^3$ reflective particles of macroscopic (mm) size immersed in an optically active fluid. The model and the experimental system, however, differ in two aspects. Since macroscopic heavy particles sediment under gravity, a fluidlike distribution has been obtained by applying mechanical shaking. Therefore, the experimental system is out of thermal equilibrium, with both the density of particles and their dynamics being controlled by shaking and gravity. These two effects are difficult to reproduce by simulation (at least because the details of shaking and the precise state of the solvent, i.e., density, temperature, and viscosity, are not reported). Therefore, the simulation is carried out assuming thermodynamic (athermal, in the case of hard particles) equilibrium and neglecting gravity. In practice, the model is closer to the colloidal RLs than to the shaken granular system of Ref. [10]. Moreover, the model assumes that the disordered configuration of the metal spheres is probed by a thin laser beam whose waist is significantly thinner than the particles' diameter. Although the laser beam used in Ref. [10] has a waist of a few mm, the thin beam assumption of the model greatly simplifies the analysis of the light path through the model system, which corresponds to the geometric scheme in Fig. 1. Despite these two differences, we still emphasize the connection with the cited experimental paper, partly because, as in Ref. [10], our model assumes perfect reflection by sphere of diameter $\sigma \gg \lambda$, with λ being the wavelength of the input and output light. Moreover, the model

system could be readily replicated by experiments with nearly the same setup of Ref. [10], since laser beams of $\sim 50 \mu\text{m}$ waist ($\ll 2R$; see Fig. 1) are widely available.

In more detail, the simulation model consists of N isotropic particles in two or three dimensions of coordinates $\{\mathbf{R}_i, i = 1, \dots, N\}$ enclosed in an orthorhombic simulation box of size $L_x \times L_y (\times L_z)$, exposing two parallel surfaces perpendicular to the x axis, and periodically repeated in the other direction(s). Confinement within the slab is enforced through an external potential $W(R_x^i)$ acting on the particles, which vanishes for $0 \leq R_x^i \leq L_x$ and is infinitely repulsive otherwise. In what follows the term *disk* will be used for 2D particles only, while *sphere* will be used for 3D particles, but also when referring to either 2D and 3D systems without distinction.

For the sake of simplicity, we describe first the model and method for the 2D case, the extension to the 3D case being straightforward. The first model that has been simulated consists of hard disks, whose hard-core (hc) potential energy is infinite if at least two disks overlap, and zero otherwise. The system is athermal, and the properties of the homogeneous phases and interfaces with confining hard walls (as in the present simulations) are well documented in the literature [43,44]. For monodisperse homogeneous samples, all properties are functions of a single parameter i.e., the packing fraction $\eta = \frac{\pi}{4} \rho \sigma^2$, where ρ is the number density. The homogeneous fluid phase is stable up to $\eta_F \sim 0.699$, separated from the hexagonal compact 2D crystal phase (stable for $\eta > 0.723$) by the hexatic phase [43]. The highest (close) packing is $\eta_{cp} = \pi/\sqrt{12} = 0.906899$. The amorphous phase might form by rapid compression of samples, but in monodisperse systems solidification into a defective crystal is the most likely result of increasing the density beyond η_F .

To cover also the liquid-vapor equilibrium, and especially the existence of a critical point, whose fluctuations might pose a particular challenge to simpler models of light propagation, simulations have also been carried out for 2D hard particles with an attractive potential well of depth $-\epsilon$ and amplitude δ :

$$v(r) = \begin{cases} \infty & r \leq \sigma \\ -\epsilon & \sigma < r \leq \sigma + \delta. \\ 0 & \text{otherwise} \end{cases} \quad (1)$$

The particle-wall interaction $W(x)$ is still purely hard wall.

This model is no longer athermal, and we explored a few thermodynamic states in the (η, T) plane. The choice of these two parameters for this second 2D system has been guided by the simulation results of Ref. [45], considering, in particular, states close to the critical point of this model. Similar computations have been done for the 3D analog of the force field model of Eq. (1). In this second case, the critical point data of Ref. [46] have been used.

In all simulated cases, in both two and three dimensions, with and without the attractive potential well, particles are assumed to be fully reflective at the surface of their hard sphere potential.

For each system and choice of the thermodynamic conditions, n independent configurations have been extracted from a MC simulation. For the hard sphere plus square well system, the equilibration of the sample before selecting configurations has been verified by looking at the drift of the potential energy,

and the independence of the selected configurations has been assessed by estimating the potential energy autocorrelation time. For the pure hard disk model, the potential energy is constant and the validation has been carried out by computing the mean square displacement of particles as a function of MC time, making sure that, on average, particles explore a sufficient portion of space to achieve equilibration and that the n representative configurations are independent.

Each of the selected configurations has been used to generate $m \gg 1$ paths for the propagation of light starting from the left of the slab, undergoing scattering events inside the slab, and exiting on the left (reflected) or on the right (transmitted) side of the sample [see Fig. 1(a)]. Here the assumption is that the motion of particles is so slow that the m light paths are computed at fixed position of the particles. Moreover, the beam of light is significantly thinner than the (macroscopic) particles' diameter, and the overall picture corresponds to the scheme in Fig. 1. Then the beam scattering by the macroscopic reflecting particles is computed according to geometric optics.

First, let us consider a single scattering event where a ray of incident radiation interacts with a scattering center. Since the spheres under consideration have a diameter $\sigma \gg \lambda$ where λ is the wavelength of the light, we can consider the scattering centers as circular mirrors, and each interaction of a ray with a center follows in accordance with specular reflection.

A beam of light propagating through the medium is represented by a straight line, given in the parametric form

$$\begin{aligned} x(t) &= x_0 + k_x(t - t_0), \\ y(t) &= y_0 + k_y(t - t_0), \end{aligned} \quad (2)$$

where $\mathbf{k} \equiv (k_x, k_y)$ is a unit ($k_x^2 + k_y^2 = 1$) propagation vector, and t_0 is an arbitrary starting parameter. For simplicity, we will think of t as time, and visualize light as traveling along the line at unit speed in the direction of increasing t . In other terms, we imagine light moving as a thin beam, whose front is far less extended than the (macroscopic) size of the particles.

In our analysis the light beam starts at position $(x_0 = -\sigma/2; y_0)$, where y_0 is a random number selected as specified in the Results section. The initial propagation vector is $\mathbf{k} = \mathbf{k}_0 \equiv (1; 0)$. During propagation in the random medium, traveling in the generic $(k_x; k_y)$ direction following a scattering event at position $(x_r; y_r)$, the time dependence of the beam location is given by

$$\begin{aligned} x(t) &= x_r + k_x t, \\ y(t) &= y_r + k_y t, \end{aligned} \quad (3)$$

where the origin of time has been shifted to the time of the previous scattering event. Elementary geometric considerations show that the distance between the center (R_x^i, R_y^i) of disk i and the straight propagation line is

$$d_{\min} = \sqrt{d_0^2 - [k_x(R_x - x_r) + k_y(R_y - y_r)]^2}, \quad (4)$$

where d_0 is the separation of $(x_r; y_r)$ from (R_x^i, R_y^i) , and occurs at

$$t_{\min} = k_x(x_r - R_x) + k_y(y_r - R_y). \quad (5)$$

The beam intersects the surface of the same sphere provided $d_{\min} \leq (\sigma/2)^2$, and the intersection [see Fig. 1(b)] occurs at

$$t_s = t_{\min} - \sqrt{\frac{\sigma^2}{4} - d_{\min}^2}. \quad (6)$$

The intersection is relevant only if $t_s \geq 0$. Then the location of the following scattering event is identified as $(x_r + k_x \bar{t}_s, y_r + k_y \bar{t}_s)$ where \bar{t}_s is the minimum among the positive beam-surface intersection times with respect to all particles.

The radius \mathbf{R} joining the center of the scattering sphere to the scattering point on its surface is orthogonal to the surface. The incoming propagation vector \mathbf{k} is projected into its components parallel (\mathbf{k}^{\parallel}) and perpendicular (\mathbf{k}^{\perp}) to \mathbf{R} . The outgoing propagation vector \mathbf{k}' is obtained by conserving the parallel component and reversing the perpendicular one:

$$\mathbf{k}' = \mathbf{k}^{\parallel} - \mathbf{k}^{\perp}. \quad (7)$$

Starting from the initial position $(x_0 = -\sigma/2, y_0)$ and propagation vector $\mathbf{k}_0 \equiv (1; 0)$ of the beam, scattering events are identified until there is no further scattering at positive time. If, at that point, the propagation vector has a positive k_x component, the beam will exit the slab from its right interface, the path is counted as transmitted, and its length is accounted for in histograms of the properties of transmitted paths. In this case the number n_s of scattering events since the beginning of the trajectory is also recorded to compute the mean-free paths of transmitted trajectories, as detailed below. In the case that $k_x < 0$, the beam exits the slab on the initial (left) side, and the path is counted among those reflected back.

This straightforward algorithm works and is easily adapted to incorporate periodic boundary conditions in the direction(s) orthogonal to x . However, at each reflection event, it requires one to compute the particle-beam distance d_{\min} of each particle in the system (or more, considering that the beam can cross a distance $> L_y$ in the transverse direction). A measure of time savings is introduced by considering that in two dimensions, starting from the scattering point (x_r, y_r) , a beam of wave vector $(k_x > 0; k_y > 0)$ can be scattered again only by particles whose position (R_x^i, R_y^i) satisfies the conditions

$$\begin{aligned} x_r - \frac{\sigma}{2} &\leq R_x^i \leq L_x, \\ y_r - \frac{\sigma}{2} &\leq R_y^i \leq y_r + k_y \left(\frac{L_x - x_r}{k_x} \right) \end{aligned}$$

with similar conditions for different sign combinations of the components (k_x, k_y) of the scattering vector. These simple geometric conditions decrease (on average by a factor of four in two dimensions, a factor of eight in three) the number of scattering events to be checked. Although this constant and relatively small gain factor is not decisive, for sample sizes of the order of 10^3 particles the determination of light paths is sufficiently fast to allow collecting statistics over several million paths for each sample, using only a few core hours on a laptop or desktop.

All the equations reported above for 2D samples remain valid for the 3D case, with the trivial addition of the z component in all coordinate and propagation vectors, playing a role completely analogous to that of the y component. Also

the considerations on the relatively low computational cost remain valid in three dimensions.

The foremost characterization of the transmission and amplification process concerns the length l of the light paths crossing the slab after many reflections by the colloidal particles, since this quantity is directly related to amplification. Because of the inherent disorder of the distribution of scatterers, l is a random variable whose probability distribution $P(l)$ will be characterized by simple statistical parameters such as the mean value (Mean), the standard deviation (SDev), the skewness (Skew), and kurtosis, or, more precisely, the excess kurtosis (ExKur), equal to the difference between the kurtosis and the constant value (equal to 3) of the Gaussian distribution. All these parameters are simply related to scaled moments (centered on the mean value and normalized by the SDev) of the distribution up to the fourth. They are computed directly by the program that generates and analyzes the light paths in the slab.

Besides the mean value, the analysis will focus on the excess kurtosis, which measures the *tailedness* of the distribution, with positive values of ExKur (leptokurtic distribution) corresponding to an excess of positive outliers (i.e., $l \gg \langle l \rangle$) with respect to the Gaussian case. Because of the exponential character of light amplification by stimulated emission, these outliers might have a significant impact on the intensity of outgoing rays, and represent the connection with the Lévy statistics aspects [47,48] of laser emission.

An additional important parameter to consider in multiple scattering is the mean-free path, which is defined as the average distance traveled by the ray between two scattering events [49]. For a single path of length l resulting from n_s scattering events, the mean-free path is

$$l_s = \frac{l}{n_s}.$$

In the following section, the average mean-free path along trajectories crossing the sample will be determined and discussed, defined as

$$\langle l_s \rangle = \left\langle \frac{l}{n_s} \right\rangle, \quad (8)$$

where $\langle \cdot \rangle$ indicates the average over trajectories crossing the sample. A similar quantities could be computed for the paths being reflected.

A natural comparison for the $\langle l_s \rangle$ of simulation is the mean-field result:

$$\langle l_s \rangle_{mf} = \frac{1}{\rho \sigma_s}, \quad (9)$$

where σ_s is the scattering cross section of the single scatterer, and ρ is the density of scattering centers. A better semianalytical expression for $\langle l_s \rangle$ accounting for lowest order effects of particle-particle correlations is available [50]. Using this approximation, however, already requires a simulation or an approximate theory to compute the static structure factor of the particles, hence we find the simple, uncorrelated expression in Eq. (9) to be the most suitable benchmark for the computational results.

$\langle l_s \rangle$ is often used as a diagnostic index to monitor the conditions for Anderson localization [15], where it is scaled

with the wave vector of the incident light [51]. However, the present investigation is purely geometric and the model does not display any nonlinearity, hence Anderson localization is beyond the scope of the present study. We can instead use the parameter l_s as a single-parameter characterization of the diffusive medium through which the light travels. There are typically three regimes to describe multiple scattering: localization, diffusive, and ballistic [49]. In most cases, i.e., when the density is not too low, the propagation of light in the samples we considered occurs in the diffusive regime, where photons propagate according to the diffusion equation [49].

Another valuable parameter of the simulation is the amplification ratio of the output light to the input light. The present study, however, is focused on the light propagation in the disordered medium filling the slab, while amplification is discussed only *a posteriori*, on the basis of the results for the geometric trajectories. Wave-dependent aspects such as interference and diffraction are neglected, and also neglected is the quantum nature of photon statistics and stimulated emission. In this simplified picture, each incoming ray carries the input intensity i_0 . Provided amplification is low, the output intensity I_{out} of a ray going through the slab is estimated as

$$I_{\text{out}} = i_0 e^{\beta \langle l \rangle}, \quad (10)$$

where $\langle l \rangle$ is the average path length of transmitted rays and β is the gain per unit length of the active fluid medium. To estimate the order of magnitude of a few quantities, the value $\beta = 0.002$ will be used, being clear that this value is arbitrary and large, considering the unit of length adopted in this study, equal to the (presumably small) diameter σ of particles. In reality, the value would depend on the physical parameters of the experiment, such as the chemical composition and concentration of the solution used and the size of the sample. If N rays are sent through the slab, then the input intensity is Ni_0 . On the other side of the slab we have $j \ll N$ rays with an energy of $i_0 e^{\beta \langle l \rangle}$. Therefore, the amplification ratio is

$$k_{\text{ampl}} = \frac{j}{N} e^{\beta \langle l \rangle}. \quad (11)$$

These parameters and properties are discussed in more detail in Sec. III.

III. RESULTS

A. Colloidal particle configurations

The first step in the simulation protocol has been to create random configurations of hard disks and spheres of unit diameter ($\sigma = 1$) over a wide range of packing fractions. In the 2D case, for instance, as many nonoverlapping disks as possible were packed into a square of side $L = 40\sigma$. Using a random number generator, a sequence of (x_i, y_i) centers were created, each time rejecting any disks overlapping with those already in the system. The maximum number of disks we could pack into the square was $N = 1034$, corresponding to a packing fraction of $\eta = 0.537$. Then a sequence of 11 samples spanning $0.01 \leq \eta \leq 0.5$ has been generated by expanding the box side to $L_x = L_y = \frac{\sigma}{2} \sqrt{N\pi/\eta}$. The list of packing fractions that have been simulated is $\eta \in [0.01; 0.05 \times j; j = 1, \dots, 10]$. A similar procedure in three dimensions results in a sequence of 11 samples at the same $\eta (= \frac{\pi}{6} \rho \sigma^3)$ of the 2D case, but

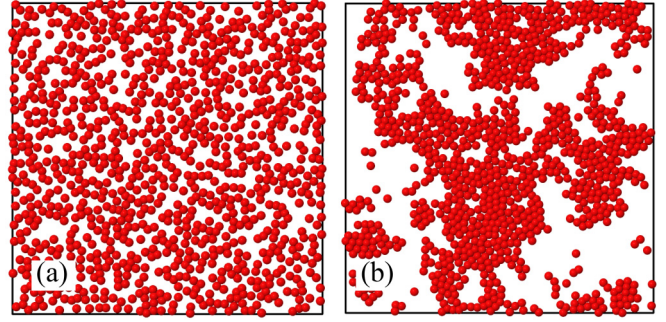


FIG. 2. Snapshot of the simulation cell for two 2D systems: (a) the pure hard disk sample at $\eta = 0.3$ and (b) the hard disk plus attractive square well potential in proximity of the critical point of the model at $\eta^* = 0.2751$ and $T^* = 0.5546\epsilon$. In (b) the strength of the attractive potential well is $\epsilon = 1$, and the attractive square well extends over the interval $1 \leq r/\sigma \leq 1.5$. Both samples consist of 1034 particles, are finite along the horizontal x direction, and are periodic along the orthogonal y direction. The radius of the dots and the side of the cell are at scale.

consisting of 5039 spheres, a size somewhat larger but still comparable to that of the experimental sample in Ref. [10]. Each sample in two and in three dimensions has been equilibrated by Monte Carlo for a number of steps ranging from 200×10^6 at $\eta = 0.01$ to 10^9 at $\eta = 0.5$. A further MC run of 40×10^6 steps has been used to generate 201 independent configurations per sample on which the analysis of light propagation has been carried out.

The starting configurations for the 2D and 3D hard particles are suitable to initiate simulations also for the system made of particles with the square well attractive tail, since the two models share the same hard-core radius. Then, the equilibration and the generation of the 201 independent configurations for the second model potential have been carried out in the same way as for the pure hc samples. Both in two and three dimensions, samples have been considered for the attractive tail model, whose $(\rho; T)$'s belong to the critical isotherm for the two dimensionalities. The relevance of density fluctuations in proximity of the 2D critical state can be appreciated in Fig. 2. The morphology in Figs. 2(a) and 2(b), in particular, displays the characteristic features of negatively [Fig. 2(a)] and positively [Fig. 2(b)] correlated random structures [52].

To isolate the effect of the slab surfaces, samples of the same size and number of particles have been generated by applying pbc in all directions. These samples, therefore, are homogeneous and lack both the density variation at the hard-wall surface, and the enhanced correlations parallel to the surface that have been discussed in a number of models. Also in this case both 2D and 3D samples have been considered, with and without the attractive potential well, and simulated following the same protocol of the previous cases. Then the difference in the light propagation properties of homogeneous and finite-width samples is attributed to the presence of the hard-wall surfaces.

A final set of 2D samples has been generated adding a degree of polydispersivity to the population of particles. The polydispersivity has been obtained by assigning the radius of

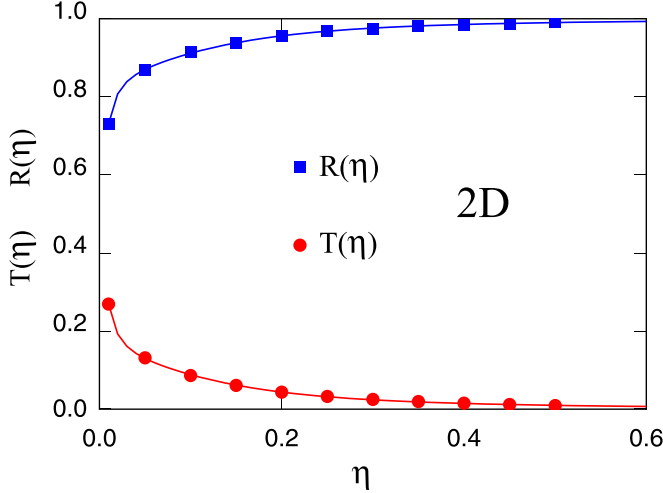


FIG. 3. Transmission (T , red dots) and reflection (R blue squares) coefficients for the 2D slabs of purely repulsive hc particles as a function of packing fraction η . The full lines are the fit described by Eq. (13). The number of particles is the same in all samples; therefore, the linear size of the slab decreases with increasing η like $L \propto \eta^{-1/2}$.

each particle according to

$$\sigma_i = 0.95 \sigma_0 + 0.1 \sigma_0 \zeta, \quad (12)$$

where $\sigma_0 = 1$ and ζ is a random variable linearly distributed in $]0; 1[$. The size L of each sample has been rescaled to obtain the same η values of the previous models.

B. Analysis of light trajectories

The preparation of configurations and the analysis of light paths arguably are simplest for the case of the pure hard disks in two dimensions. For this reason we discuss first the results for this case, which represent a clear benchmark for all the other systems that have been investigated. The analysis is based on the generation of at least one million light paths for each of the 201 independent configurations ($>201 \times 10^6$ paths per sample) selected from the MC run of the 11 samples spanning the $0.01 \leq \eta \leq 0.5$ packing fraction range.

Preliminary to the discussion of all other properties, the transmission coefficient T and the reflection coefficient R are reported as a concise characterization of the overall effect of the slab on the incident beam. These coefficients are defined in purely geometric terms, neglecting amplification by stimulated emission and absorption by the fluid medium. Then T is the fraction of light rays crossing the slab, while R is the fraction of light rays being reflected back to the original half space, with $T + R = 1$. The results shown in Fig. 3 follow intuition. At low η , R is expected to grow linearly starting from its $\lim_{\eta \rightarrow 0} R(\eta) = 0$ and to tend to 1 with increasing η , without reaching it within the density range of fluid hard disk systems. The simple Padé form

$$R(\eta) = \frac{A\eta + B\eta^3}{1 + C\eta + B\eta^3} \quad (13)$$

provides an excellent fit of the data for R , and it can be trivially rewritten for $T = 1 - R$. Assuming that the functional form

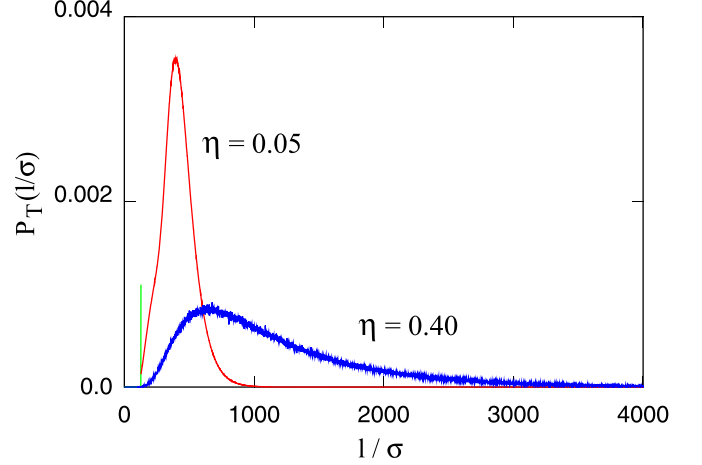


FIG. 4. Probability distribution $P_T(l)$ of the length l of the light path crossing the 2D slab. Particles interact with each other and with the confining wall by purely hc interactions. The vertical green line belongs to the $\eta = 0.05$ data and represents the fraction of light rays of length $l = L_x$ crossing the slab without being scattered.

reflects the true dependence of R on η , it is easy to verify that the deviation of R from 1 decreases like η^{-2} with increasing η , and, equivalently, T decreases like the same η^{-2} with increasing η . Needless to say, considerations on asymptotic trends are not very relevant in this context, since the admissible range of η is limited to $\eta \leq \eta_{cp}$. Apart from these general properties, the detailed values of T and R as a function of η depend on the thickness of the slab. For the size of the simulated systems, it is apparent that the fraction of beams transmitted through the slab decreases very quickly at first, dropping below 10% already at $\eta = 0.1$, then (necessarily) decreasing slowly with further increase of η .

The property that more closely reflects the scattering process of light in the slab is the length l of light paths. As stated in Sec. II, this is a stochastic variable, characterized by the probability distribution $P(l)$. To be precise, the analysis is carried out separately for transmitted and reflected paths, corresponding to two probability distributions $P_T(l)$ and $P_R(l)$, respectively.

The data for transmitted paths are discussed first. The generation of at least a few hundred million paths per sample allows us to draw very accurate histograms of the paths' length, whose normalized version is the $P_T(l)$ shown in Fig. 4 for $\eta = 0.05$ and $\eta = 0.4$.

The trends apparent in the figure are very intuitive. First, no transmitted path can be shorter than the width L_x of the slab, hence $P_T(l) = 0$ if $l < L_x$. The sharp peak at $l = L_x$ in the plot for $\eta = 0.05$ corresponds to rays crossing the slab without being scattered. This peak quickly becomes negligible with increasing η . To emphasize these features, the distribution $P_T(l)$ is rewritten as

$$P_T(l) = \begin{cases} 0 & l < L_x \\ x\delta(l - L_x) & l = L_x, \\ (1-x)\bar{P}_T(l) & l > L_x \end{cases} \quad (14)$$

where $0 \leq x \leq 1$ is the relative weight of the δ -like peak. The continuous portion $\bar{P}_T(l)$ of the distribution, whose

TABLE I. Mean value (Mean), standard deviation (SDev), skewness (Skew), and excess kurtosis (ExKur) of the probability distribution $P_T(l)$ for the length l of transmitted paths in 2D samples of hard disks as a function of the packing fraction η . The corresponding values obtained by the fit of the continuous part $\bar{P}_T(l)$ of $P_T(l)$ with an inverse Gaussian distribution are listed in parentheses. The fit parameter have been omitted for $\eta = 0.01$ because in that case the fit is not even qualitatively close to the simulation data. Statistical error bars are implicitly indicated by the number of digits of the data.

Transmitted Path Length Distribution: Statistical Moments											
η	0.01	0.05	0.1	0.15	0.2	0.25	0.3	0.35	0.4	0.45	0.5
Mean	658 (—)	416 (452)	386 (391)	455 (454)	618 (639)	798 (840)	928 (963)	1046 (1076)	1172 (1200)	1333 (1360)	1521 (1548)
SDev	302 (—)	128 (139)	140 (135)	223 (219)	370 (412)	507 (582)	590 (654)	665 (724)	745 (802)	851 (904)	969 (1027)
Skew	0.686 (—)	0.574 (1.29)	1.36 (1.35)	1.70 (1.73)	1.77 (2.15)	1.79 (2.23)	1.81 (2.15)	1.80 (2.11)	1.79 (2.08)	1.81 (2.06)	1.80 (2.04)
ExcKur	0.1 (—)	1.07 (2.77)	3.40 (3.02)	4.7 (5.00)	4.9 (7.71)	5.1 (8.29)	5.2 (7.72)	5.1 (7.43)	5.0 (7.22)	5.2 (7.07)	5.1 (6.96)

normalization is one, is skewed right, and, with increasing η , it becomes broader and moves toward larger l 's, despite the progressive shrinking of the slab.

The qualitative results obtained by visual inspection of the $P_T(l)$ distributions are quantified by computing the average path length $\langle l \rangle$, the variance, skewness, and kurtosis of the length distribution of all samples. The parameters collected in Table I show that for $\eta \geq 0.1$ the mean value and the standard deviation increase rapidly with increasing η , while both skewness and excess kurtosis saturate to a constant value from below. The excess kurtosis, which is of particular interest for the present discussion, is always positive and sizable, implying that the distribution has an excess of outliers with respect to the Gaussian distribution. To be precise, the average length has a nonmonotonic behavior, at first decreasing in a narrow interval of η , with a minimum at $\eta \sim 0.1$ (see Fig. 5). The presence of the minimum has to be expected since, at constant number of particles, the linear size of the system,

and therefore the minimum path length, diverge in the $\eta \rightarrow 0$ limit, while at large η the value of l increases again because of trapping of light into the slab.

While the δ -like peak is relevant only at low η and its weight x is difficult to predict, a few more observations can be made on the continuous part $\bar{P}_T(l)$ of the distribution. First, one can remark that as soon as the density of scattering centers is non-negligible, the light paths inside the slab resemble the trajectory of a random walk. The length l of each of the transmitted paths is equivalent to the time t spent by a Brownian particle to travel at unit velocity from $(-\sigma/2, y_0)$ to the exit point having $x = L_x$ (irrespective of the y exit coordinate). The distribution of these times has a vague relation with the Wald distribution P_W , also known as the inverse Gaussian distribution:

$$P_W(t \equiv l; \mu, \lambda) = \sqrt{\frac{\lambda}{2\pi t^3}} \exp\left[-\frac{\lambda(t - \mu)^2}{2\mu^2 t}\right], \quad (15)$$

which describes the distribution of times taken by a Brownian particle to travel a given distance. In Eq. (15), μ is the average value and λ is a fit parameter closely related to the variance of the distribution. Admittedly, because of the spread of the y exit coordinate along the surface plane, the random variable l measured in the simulation is not the time needed to a Brownian particle to drift by the distance L_x , therefore, Eq. (15) cannot be the *a priori* model that describes the simulation results. Nevertheless, we verified that Eq. (15) still represents a suitable analytical form to fit the simulation results, provided the density of scattering centers is not too low.

To be precise, the expression of Eq. (15) cannot reproduce the simulation data because, as already remarked, no transmitted path can be shorter than the width L of the slab, and $P(l)$ has to be zero for $l < L$.

To enforce this condition, the smooth part of the probability distribution is modeled as

$$\bar{P}_T(l) = \begin{cases} 0 & l < L_x \\ P_W(l - L_x) & l \geq L_x \end{cases}, \quad (16)$$

where P_W is the Wald distribution of Eq. (15). The rigid shift by L_x changes the average $\langle l \rangle$ from μ to $\mu + L_x$, but it does not change the estimate of the variance μ^3/λ , skewness $3\sqrt{\mu/\lambda}$, and excess kurtosis $15\mu/\lambda$.

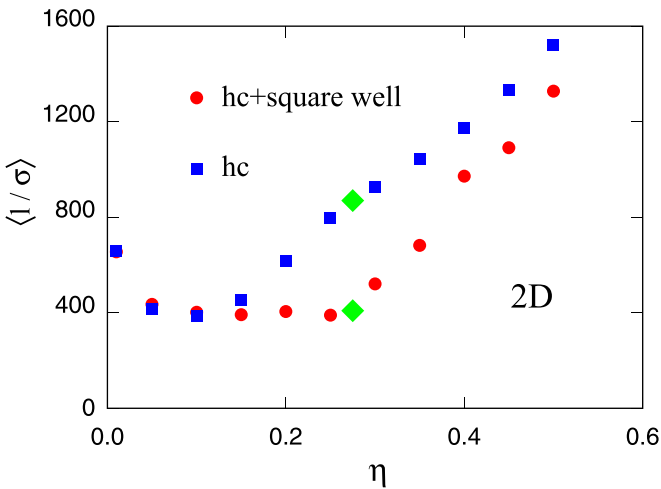


FIG. 5. Average length $\langle l \rangle$ of transmitted paths as a function of η . Blue filled squares: hc potential; red dots: hc plus attractive square well tail. Green diamonds mark the values at the η of the critical point for the 2D hc plus the attractive square well potential described in the text.

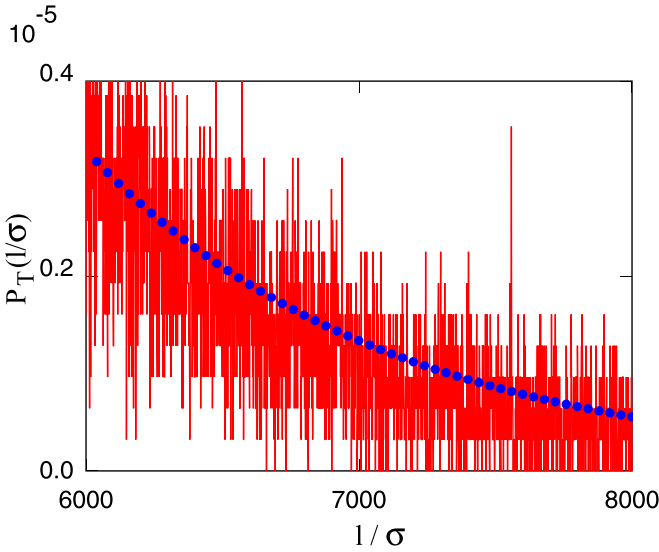


FIG. 6. Long- l tail of the probability distribution $P(l)$ of light path crossing the 2D slab at $\eta = 0.5$. Comparison of fit (blue dots) and raw data (red line).

As soon as η exceed ~ 0.1 , the inverse Gaussian distribution of Eq. (16) provides an excellent fit of the entire distribution given by simulation (see Fig. S1 in the Supplemental Material [53]), allowing an immediate estimate of average, standard deviation, skewness, and excess kurtosis, whose values are close to those computed directly by the simulation (see Table I). In the medium- and high-density range, the ability of the inverse Gaussian distribution to fit the simulation data extends to high l , as shown in Fig. 6. This observation is remarkable, since the tail of the distribution has a negligible weight in the fit. Perhaps more importantly, the analytical expression of the fit distribution allows us to derive the asymptotic distribution of the output power, following amplification by the optically active medium. This aspect is discussed in Sec. III E.

It is apparent, however, that at low η the inverse Gaussian distribution differs even qualitatively from the simulation data, as shown in Fig. 7 for the $\eta = 0.01$ case. The reason of the discrepancy between simulation data and inverse Gaussian fit at low η is easy to guess and verify through the data analysis. The usage of the inverse Gaussian distribution relies on the underlying diffusive dynamics for the propagation of light in the slab, which, in turn, implies a multitude of scattering events to approach a genuine Brownian process. At low η , instead, a sizable number of paths cross the slab without being scattered, and many other paths are scattered only a limited number of times, thus the limit of a Brownian process is not reached. This interpretation is verified in the inset of Fig. 7(b), showing the contribution to $P(l)$ from paths that cross the slab undergoing ≤ 6 and >6 scattering events. The two sets of paths seem to represent different populations, accounting for the bimodal character of the distribution, that cannot be reproduced by the inverse Gaussian analytical expression.

Turning now to the properties of the reflected rays: for all 2D hard disk samples, the probability distribution $P_R(l)$ for the length l of the reflected rays decays monotonically as a

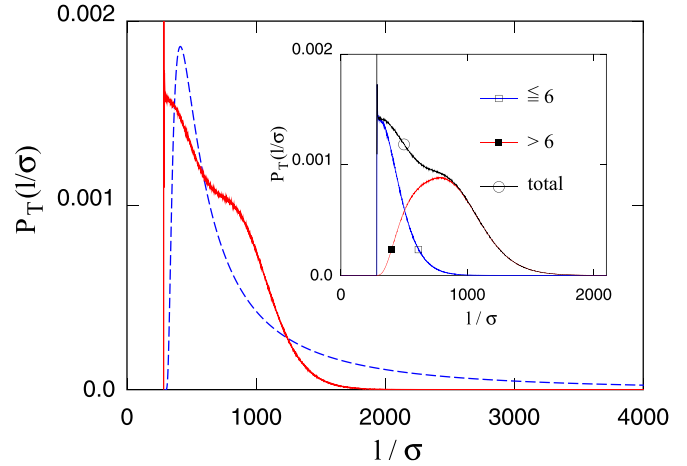


FIG. 7. Main panel: Probability distribution $P(l)$ of the length l of the light path crossing the 2D slab at $\eta = 0.01$. Comparison of fit (dashed line) and simulation data (full line). The inset shows the breakdown of the simulation data into contribution from paths undergoing ≤ 6 and >6 scattering events while crossing the slab. The different curves are identified by the symbols on the lines, as specified in the figure.

function of l . Moreover, the average path length $\langle l \rangle_R$ decreases monotonically with increasing η (see Table II). The decrease is very rapid at first, then the value nearly saturates for $\eta \geq 0.30$, apparently because of the compensation between the increasing reflectivity of the slab, which reduces $\langle l \rangle_R$, and the increasing length of any path that is able to penetrate beyond the first layer of colloidal particles before being reflected back.

A logarithmic plot of $P_R(l)$ suggests the functional form

$$P_R(l) = \frac{A}{1 + Bl^{1/2} + Cl^{3/2}} \quad (17)$$

as resembling the simulation data at all values of η . The numerical fit is reasonably accurate, but admittedly the fit is empirical and not as good as the inverse Gaussian distribution for $P_T(l)$. On the other hand, a fit with a sum of exponentials does not achieve the same χ^2 (accounting for the number of degrees of freedom in the fit). It might be useful to remark that $P_T(l)$ does not measure nor it is directly related to the penetration depth of the rays into the slab.

The mean-free path $\langle l_s \rangle$ defined as the average length of linear segments between scattering events decreases monotonically with increasing η . A fit with a simple inverse power of η ($\langle l_s \rangle = A/\eta$), following the mean-field result, reproduces

TABLE II. Mean value (Mean) and standard deviation (SDev) of the probability distribution $P_R(l)$ for the length l of reflected paths in 2D samples of hard disks as a function of the packing fraction η . Statistical error bars are implicitly indicated by the number of digits of the data.

Reflected Path Length Distribution: Statistical Moments											
η	0.01	0.05	0.1	0.15	0.2	0.25	0.3	0.35	0.4	0.45	0.5
Mean	320	120	80	70	67	66	62	59	57	57	56
SDev	330	150	125	140	170	200	210	220	225	240	255

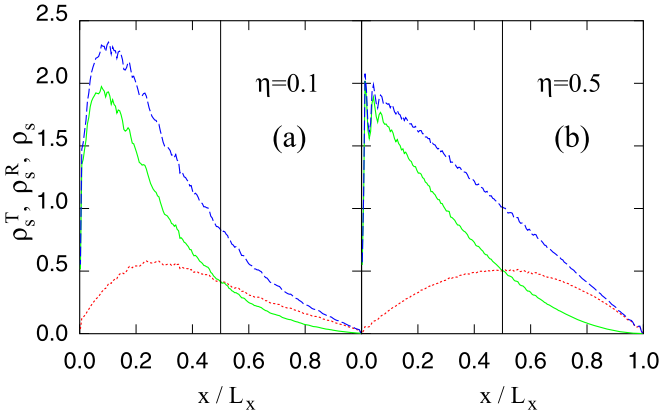


FIG. 8. Probability density of scattering events across a 2D slab whose particles interact via a purely hc potential. Red dotted line: $\rho_s^T(x)$; green line: $\rho_s^R(x)$; blue dashed line: $\rho_s(x) = \rho_s^T(x) + \rho_s^R(x)$.

the simulation data fairly well. A significant further reduction of the square deviation and of χ^2 is obtained by adding a logarithmic term, i.e., $\langle l_s \rangle = A/\eta + B/\log(\eta)$, that apparently arises from effects beyond mean field. The monotonic decrease of $\langle l_s \rangle$ and the nonmonotonicity of $\langle l \rangle$ vs η can be matched by considering that the number of scattering events experienced by a beam transmitted through the slab increases slowly at first, and then more rapidly with increasing η , as verified by the simulation data. To a very good approximation, these properties of the mean-free path are shared by transmitted and reflected trajectories.

Given the inhomogeneous and asymmetric nature of the system and process, it is of interest to determine where the scattering events take place along the coordinate x normal to the slab. This information is contained in the density distribution $\rho_s(x)$ of scattering events, shown in Figs. 8(a) and 8(b), at low and high η , respectively. The properties of the system are easier to understand at high η such that the propagation of light is diffusive. In such a case, the propagation of light is similar to many other transport processes based on diffusion with a superimposed slight drift, such as electric and thermal conductivity, driven by an electrostatic potential and temperature difference, respectively. In the present case, the potential is represented by the light intensity $I(x, t)$ (where t is time), and the resistance is due to the scattering processes, which limit the flow of the light current $J(x, t) = k [dI(x, t)/dx]$, which, because of light intensity conservation, satisfies a continuity equation. In the previous relation, k is the light conductivity. At stationary conditions, $J(x, t)$ is constant along x and t , reflecting the constant gradient of the light intensity within the slab along x . In other terms, at stationary conditions, the light intensity $I(x)$ decreases linearly with x . Neglecting possible deviations due to the layering of particles along x in proximity of the hard walls, the density $\rho_s(x)$ of scattering events is proportional to the light intensity $I(x)$, hence the probability distribution $\rho_s(x)$ of scattering events (considering both transmitted and reflected paths) has to decrease linearly from left to right across the slab. This qualitative picture is born out by the simulation results at high η , reported in Fig. 8(b), showing a clear linear dependence of $\rho_s(x)$ on x . The picture, however, is violated at low η [see

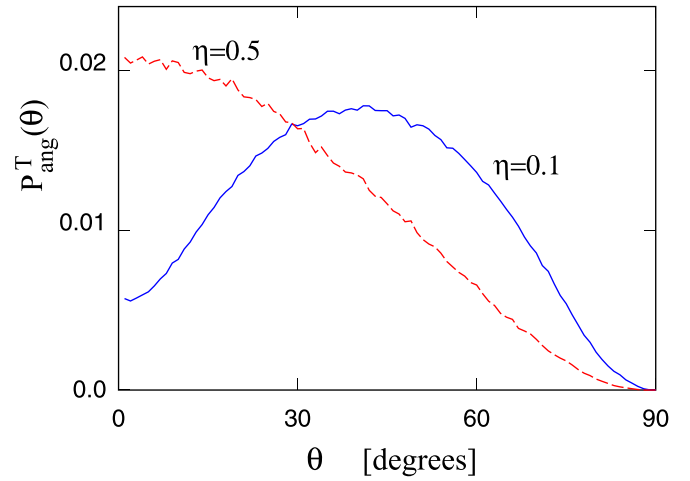


FIG. 9. Probability distribution of the exit angle θ of transmitted rays through 2D samples measured with respect to \hat{x} . Blue full line: $\eta = 0.1$; red dashed line: $\eta = 0.5$.

Fig. 8(a)] since in that case, the propagation of light is at least partly ballistic, and the influence of the interfaces extends to a sizable portion of the whole system.

More telling is the partitioning of $\rho_s(x)$ into the contributions $\rho_s^T(x)$ and $\rho_s^R(x)$, counting the number of scattering events arising from transmitted and reflected paths, respectively. In the diffusive regime, paths at the geometric center of the slab have nearly the same probability of exiting on the left and on the right of the slab. Therefore, to a good approximation, $\rho_s^T(L_x/2) = \rho_s^R(L_x/2)$, provided the propagation is diffusive. A slight unbalance might be due to the random position of the colloidal particles, and especially to the weak constant flow J crossing the slab from left to right.

Furthermore, $\rho_s^T(x)$ has to be nearly symmetric around $x = L_x/2$, with $d\rho_s^T(x)/dx = 0$, since transmitted paths can be traversed in both directions, hence the population of transmitted paths is the same in the right and left directions, and the same distribution of scattering events is shared by the propagation from left to right and *vice versa*. The only distinction between the left and right of $\rho_s^T(x)$ is in the boundary conditions and in the net flow J , which do not affect the details of the scattering distribution far from the surface walls, always provided η is high and the light propagation diffusive. At low η , the symmetry-breaking current J is high, the effect of the walls is less screened close to the surfaces, and the asymmetry in $\rho_s^T(x)$ is sizable, as shown in Fig. 8(a). Besides these qualitative features, the quantitative details of $\rho_s^T(x)$ and $\rho_s^R(x)$ are determined by the strength of the scattering processes, which depends on η , and by the boundary conditions, including the fact that $\rho_s^R(x)$ has to vanish at $x = L_x$.

The direction of the outgoing rays is an important aspect in view of applications of the system as random laser. For transmitted rays, the simulation results show that at low η the probability distribution $P_{ang}^T(\theta)$ of angles θ with respect to the \hat{x} direction presents a broad peak around $\theta = 45^\circ$, and a non-negligible value in the forward direction, $\theta = 0^\circ$ (see Fig. 9). At $\eta > 0.4$, the $P_{ang}^T(\theta)$ distribution is peaked at $\theta = 0^\circ$ but still broad. It has been verified that path lengths l and exit direction θ are uncorrelated. Directional beams, therefore, can

be obtained only by collimation, sacrificing most of the intensity. For reflected rays, the probability distribution $P_{ang}^R(\theta)$ of the angle θ is as broad as for the transmitted ones, but, especially at low η , it peaks at 180° , possibly because their direction is less randomized before leaving the slab. This is supported by the fact that at high η , when the beam undergoes a higher number of scattering events in the skin-depth subsurface layer before being back-reflected, the 180° peak is less pronounced than at low η (see Fig. S2 in Ref. [53]).

Analysis of the simulation trajectories shows that the propagation direction does not lose its memory at every step, as assumed by the simplest random walk models, nor it is equal to the average scattering angle from the single isolated scatterer. In the simulations the autocorrelation function of the propagation unit vector \mathbf{k} shows a limited memory, lasting a few scattering events. At densities $\eta \geq 0.01$, in particular, the average $\langle \mathbf{k} \cdot \mathbf{k}' \rangle$ for propagation vectors separated by one scattering event is negative for both transmitted and reflected rays. In other terms, the short time correlation function of propagation vectors is dominated by backscattering both along transmitted and reflected trajectories. This feature has to change at very low density, since in the limit of a single scattering sphere the same autocorrelation function can be computed analytically and (obviously) it is positive for transmitted paths, and negative for reflected paths, as we also verified numerically going to very low η . The same $\langle \mathbf{k} \cdot \mathbf{k}' \rangle$ resulting from each scattering event in a colloidal solution is discussed experimentally in Ref. [54].

One of the remarkable aspects of hc fluids confined by hard walls is the density pile up at the interface (see Fig. S3 in Ref. [53]), due to the requirement of mechanical stability ($p_{xx}(x) = \text{const}$, where p_{xx} is the xx element of the stress tensor) across the slab [55]. In these systems, the peak density at contact increases rapidly with increasing packing fraction, and at high η it might severely hamper the penetration of light into the slab, increasing its reflectivity. To quantify this effect, comparison has been made with the results computed for a sample of the same size and packing, but rendered homogeneous by the application of pbc in all directions. It turns out that the overall effect, measured, for instance, by the transmission and reflection coefficients, or by the average length of transmitted and reflected path, is small at all η , partly because at the high η at which the density pile up is most important, the transmission of light through the slab is already effectively suppressed by the high average particle density. The effect on the microscopic scattering mechanisms, however, is important, and easily identified by the computation. The comparison of the distribution of scattering events, for instance, shown in Fig. 10, shows an important change in the fine structure of $\rho_s(x)$ in proximity of the interface. The value of $\rho_s(x)$ is a measure of the light intensity at position x . The slightly lower value of $\rho_s(x)$ well inside the sample (see again Fig. 10) is due to the higher reflectivity of the inhomogeneous slab, although the effect integrated over the slab width L_x is only minor.

The last remark on hc 2D systems concerns the effect of polydispersity, which has been modeled as specified by Eq. (12). Also in this case, the effect grows slowly with increasing η , but it is small at all η 's that have been simulated. At $\eta = 0.5$, for instance, both the transmission coefficient and

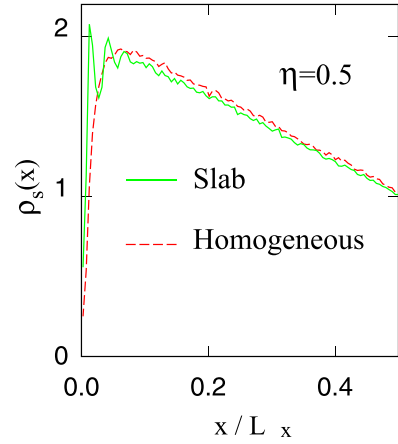


FIG. 10. Probability distribution of scattering events across the slab (green full line) and the homogeneous sample (red dashed line) for $\eta = 0.5$. The reported $\rho_s(x)$ refers to the total number of scattering events, belonging to both reflected and transmitted light paths. Most of the change observed for $x/L_x \leq 0.1$ concerns the reflected paths.

the average path length of the polydisperse sample are about 1% higher than those of the monodisperse sample. The two trends are somewhat contradictory, since an increase of path length points to a lower transmission of light. However, the difference in both T and $\langle l \rangle$ is beyond the error bar. Perhaps more telling, the differences between mono- and polydisperse samples are systematic being similar over the entire η range, confirming that they are a genuine effect of polydispersity. We verified that especially at high density, there is a relatively weak preferential segregation of small particles at the interface, changing the reflection or transmission properties of the layered slice of the slab in contact with the hard wall, and possibly causing the changes in all the other properties.

C. Hard disks with an attractive square well tail

Monte Carlo simulations and the analysis of light trajectories have been carried out for 2D particles interacting with a hard disk potential plus an attractive tail, following the same protocol used in the case of purely hard disks. Although the two models are fairly similar, there are at least two characteristic differences. At variance from pure hard disk case, the phase diagram of the hard disk plus attractive tail potential usually (but not always, see Refs. [56,57]) has a genuine liquid phase and a critical point whose critical fluctuations might greatly affect light paths in the slab, since opalescence is precisely one manifestation of criticality. The second difference concerns the structure of the fluid at the hard wall surface. Assuming that the wall-particle potential $W(x)$ is purely hard-core, the contact density of particles $\rho(x=0) = \rho(x=L_x/2)$ depends directly on the constant value of the stress tensor element $p_{xx}(x) > 0$ across the slab in the direction orthogonal to its surface. In the purely hard disk case, pressure tends to be high, and the interface is an accumulation point for particles. Density, therefore, has a peak at the interface and decays towards the bulk value with wide amplitude oscillations. For particles interacting with the hc plus attractive tail, the value of p_{xx} tends to be moderate up to fairly high η , the interface is

depleted of particles, and the density does not display short-wavelength oscillations at contact (see Fig. S3 in Ref. [53]). These differences in the liquid structure, although localized at the interfaces, might affect the transmission and reflection coefficients of the whole slab.

Simulations, in particular, have been carried out for the system having $\delta = 0.5\sigma$ [see Eq. (1)] with $\epsilon = 1$ being the unit of energy. According to Ref. [45], the critical point of this model is located at $\eta^* = 0.2751$ and $T^{ast}/\epsilon = 0.5546$. Since exploring the entire phase diagram is time consuming and possibly not very informative, a series of simulations at the same η values of the hc system have been carried out following the critical isotherm $T^{ast}/\epsilon = 0.5546$. In this way the system is always fluid and homogeneous, but in a narrow range around the critical density, it explores in a continuous way the change from a gas or vapor to a liquid state.

It turns out that heavily averaged properties of the slab such as the transmission and reflection coefficients are not greatly changed by the addition of the attractive tail, but characteristic and systematic variations are apparent around the critical density at η^* (see the comparison in Fig. S4 of Ref. [53]). However, properties more dependent on particle-particle correlations are significantly affected. Already the average length of the transmitted light rays shows important deviations from the hard disk result (see Fig. 5). As expected, differences are relatively minor at low η , where correlations are weak in both cases. Moreover, the two sets of results converge again at high $\eta \geq 0.4$, since the structure is dominated by packing effects, common to the two models. Large differences, however, are apparent at intermediate η 's where density fluctuations related to the critical state dominate the picture in the hc plus attractive tail case. Paths in the slab with attractive colloids, in particular, are markedly shorter than those in the slab with purely hc particles. The effect on the reflected paths is more uncertain, since the estimates of the $\langle l \rangle^R$ path length and of its variance fluctuate much more than the corresponding quantities measured on transmitted paths. The onset of critical opalescence is certainly not apparent in the simulation, but in experiments it is also known to occur very close to criticality, while the critical point might be much less well defined in the small, inhomogeneous systems simulated in the present study. Moreover, critical opalescence might crucially depend on fluctuations whose wavelength is much longer than the side of the simulated cell.

The difference in $\langle l \rangle$ for the two model potentials, of course, reflects a correspondingly sizable difference in the probability distribution of lengths $P_T(l)$, whose comparison is shown in Fig. S5 of Ref. [53]. In both cases $P_T(l)$ shows peculiar shapes at low η and is faithfully reproduced by the inverse Gaussian distribution at medium and high η . Besides the difference in $\langle l \rangle$, around the critical density, the $P_T(l)$ for the hc plus tail samples are systematically characterized by significantly lower variance and by slightly reduced skewness and kurtosis than the curve for purely hc systems.

Even more apparent is the difference between the two systems in the spatial probability distribution of scattering events. While the results for the hard disk samples display marked regularity and are easy to interpret, those for the sample of particles with the attractive tail display apparent irregularities at densities relatively close to the critical point [see Fig. 11(a)].

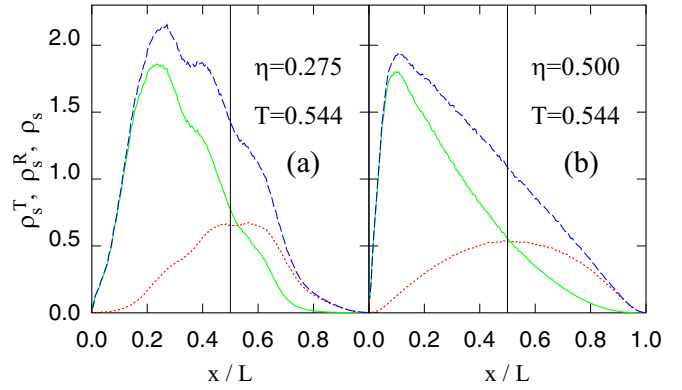


FIG. 11. Probability density of scattering events across the slab whose particles interact via an hc plus attractive tail potential. Red dashed line: $\rho_s^T(x)$; green full line: $\rho_s^R(x)$; blue dashed line: $\rho_s(x) = \rho_s^T(x) + \rho_s^R(x)$. The results for panel (a) have been obtained for a sample close to the critical state of the corresponding homogeneous system.

Detailed analysis of trajectories shows that the irregularities in ρ_s^T , ρ_s^R , ρ_s arise from the heterogeneous spatial distribution of scattering centers, and of the length of straight path segments between scattering events, as shown in Fig. 12. It is likely that these irregularities would disappear upon accumulating statistics over exceedingly long production runs, but the present simulations are already very long, and the irregularities are a clear sign that, as expected, the time to achieve equilibrium grows substantially in approaching the critical point, although any divergence is prevented by the finite (and relatively small) size of the sample. At significantly lower or higher packing, the probability distribution of scattering events resembles that of the slab with purely hc particles [see Fig. 11(b)].

It might be useful to remark that, as suggested by Fig. 12, both the fluctuations at all length scales as well as the *lacunarity* (using the terminology of Ref. [58]) of samples close to criticality are qualitatively reminiscent of those of fluids in fractal dimension (see experimental studies in Refs. [59,60] as well as Ref. [61] for an example of computational fractal structure based on particles). Therefore, the multiple-scale character of light trajectories in critical systems might also qualitatively resemble those propagating in fractal systems. A generalization of the present study to fractal dimensions, however, would be confronted to the extension of the geometric (elastic) scattering rules to particles of the same or different fractal dimension. Multiple-scale heterogeneities in the structure of the scattering centers, reflected in equally heterogeneous light trajectories, can be found in a broader class of systems; see Refs. [13,62].

D. The 3D simulations

To gain insight into the interplay of light scattering with dimensionality and interparticle correlations, the computations carried out in two dimensions have been repeated for 3D systems. In both two and three dimensions the samples are labeled by a η parameter whose definition is different but analogous in the two dimensionalities. However, using only η to establish a correspondence between two and three dimensions is somewhat incomplete, since the same sequence of η values

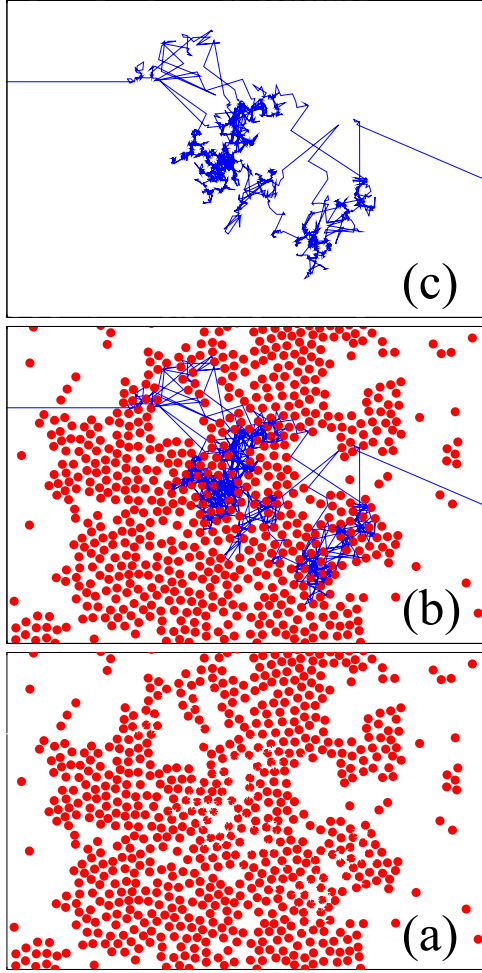


FIG. 12. (a) Snapshot of the 2D sample of hard disks (red dots) plus the attractive square well tail (see text) at conditions ($\eta = 0.3$, $T/\epsilon = 0.5546$) close to criticality. (b) Path of a ray of light (blue line) in the sample of panel (a). (c) The scattering disks have been removed to highlight the different properties of light propagation in dense and dilute domains.

spans very different sample side L or number of particle N ranges in the two cases, affecting the comparison of transmission, reflectivity, average path length, interfacial effects, etc. For instance, using in three dimensions the same number

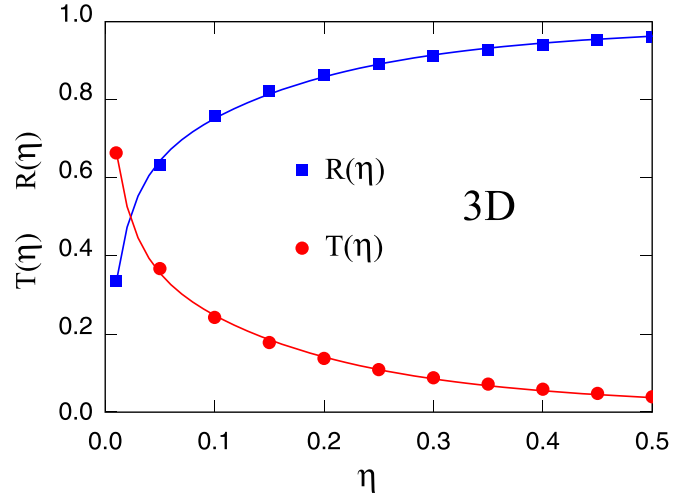


FIG. 13. Transmission (T , red dots) and reflection (R blue squares) coefficients for the 3D slabs of purely repulsive hc particles as a function of packing fraction η . The full lines are the fit described by Eq. (13). The number of particles is the same in all samples, therefore, the linear size of the slab decreases with increasing η like $L \propto \eta^{-1/3}$

of particles $N = 1034$ of the 2D systems at equal η gives 3D samples whose side L is much shorter than in two dimensions. Being impossible to balance all aspects, as a compromise, in three dimensions we adopt a somewhat larger number of particles $N = 5039$. Then the sides $L_x = L_y = L_z (\equiv L)$ of the 3D slabs have been determined in order to obtain the same sequence $\eta \in [0.01; 0.05 \times j; j = 1, \dots, 10]$ considered in two dimensions. In this way the range of 2D and 3D sides L partially overlap, although the two sequences differ from each other.

The transmission and reflection coefficient computed for the 3D samples are shown in Fig. 13. For the reasons discussed above, these data cannot be quantitatively compared to those of 2D systems. However, it is apparent that the simple Padé form of Eq. (13) (with reoptimized coefficients) provides an equally good fit of the 2D and 3D results.

The parameters characterizing the probability distribution of transmitted path lengths $P_T(l)$ in three dimensions are summarized in Table III. At variance from the 2D case, the

TABLE III. Mean value (Mean), standard deviation (SDev), skewness (Skew), and excess kurtosis (ExKur) of the probability distribution $P(l)$ for the length l of transmitted paths in 3D samples of hard spheres as a function of the packing fraction η . The corresponding values obtained by the fit of the continuous part of $P(l)$ with an inverse Gaussian distribution are listed in parentheses.

Transmitted Path Length Distribution: Statistical Moments											
η	0.01	0.05	0.1	0.15	0.2	0.25	0.3	0.35	0.4	0.45	0.5
Mean	91	98	111	124	138	153	168	186	206	228	253
	(—)	(—)	(—)	(154)	(159)	(169)	(182)	(198)	(217)	(237)	(263)
SDev	57	69	74	81	89	97	107	118	131	144	161
	(—)	(—)	(—)	(138)	(128)	(129)	(132)	(140)	(151)	(163)	(178)
Skew	3.5	2.1	1.9	1.8	1.8	1.8	1.8	1.8	1.8	1.8	1.8
	(—)	(—)	(—)	(3.2)	(2.8)	(2.6)	(2.5)	(2.4)	(2.3)	(2.2)	(2.2)
ExcKur	16.7	6.2	5.4	5.2	5.2	5.1	5.2	5.2	5.2	5.3	5.4
	(—)	(—)	(—)	(17.6)	(13.4)	(11.4)	(10.1)	(9.2)	(8.7)	(8.3)	(7.9)

TABLE IV. Mean value (Mean) and standard deviation (SDev) of the probability distribution $P_R(l)$ for the length l of reflected paths in 3D samples of hard spheres as a function of the packing fraction η . Statistical error bars are implicitly indicated by the number of digits of the data.

Reflected Path Length Distribution: Statistical Moments											
η	0.01	0.05	0.1	0.15	0.2	0.25	0.3	0.35	0.4	0.45	0.5
Mean	103	64	50	45	40	35	33	31	29	28	27
SDev	83	70	62	60	60	60	63	64	66	68	71

minimum in the average path length $\langle l \rangle$ as a function of η is not seen in the results of the 3D simulations, but the argument underlying its existence is valid also in three dimensions, and the trends in the computed data simply imply that the minimum occurs around or below the minimum packing fraction $\eta = 0.01$ simulated in the present study. Apart from this aspect, all the other trends are qualitatively the same in three as in two dimensions. On the 3D data, the effect of the δ -like peak in $P_T(l)$ at $l = L_x$ due to path crossing without being scattered is significant up to $\eta = 0.15$, apparently because of the relatively limited thickness of the slab. Neglecting this peak, at medium-high η (≥ 0.15) the inverse Gaussian distribution provides an excellent fit of the smooth part $\tilde{P}_T(l)$ of $P_T(l)$, while the fit is poor at lower η (see Fig. S6 and Fig. S7 in Ref. [53]), presumably for the same reasons discussed for the 2D case, i.e., at low η the propagation of light is not diffusive. The length distribution for reflected rays in three dimensions displays the same qualitative features of the 2D case. The main quantitative parameters are given in Table IV.

The mean-free path of rays in the colloidal suspension is the most local property of the light paths diffusing in the slab, therefore it could be compared directly for the two dimensionalities. The comparison between the mean-free path in 2D and 3D simulations is displayed in Fig. 14 for $0.2 \leq \eta \leq 0.5$. Lower values of η have been excluded because the contribution from unscattered rays is sizable and it can obscure the comparison of the diffusive contribution. One could expect

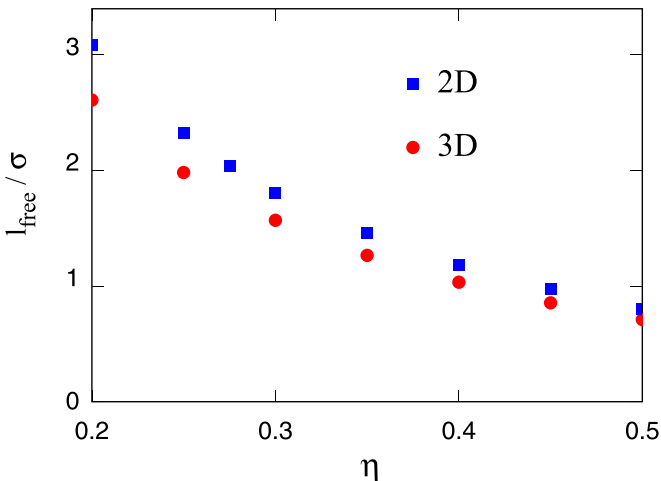


FIG. 14. Comparison of the mean-free path in two and three dimensions.

that the mean-free path is shorter in two dimensions, since localization by disorder is enhanced by reducing dimensionality [63]. Somewhat surprisingly, the mean-free path is slightly but systematically higher in 2D samples than in the 3D ones.

The dependence of the average number of scattering events experienced by transmitted rays and estimated as $n_s = \langle l \rangle / l_{\text{free}}$ is similar to that already discussed for two dimensions, i.e., the growth is slow at low η and becomes faster with increasing η . This aspect, however, might be influenced by the dependence of the scattering properties on the slab thickness L_x .

The density distribution of scattering events along the x coordinate in 3D systems is analogous to the one in two dimensions in virtually every aspect, including the near-symmetry of $\rho_s^T(x)$ around $L_x/2$, the linearity of the total $\rho_s(x)$, and its anomalies at low η . These features are illustrated in Fig. S8 of Ref. [53].

The effect of the interfaces and of the density pile up at $x = 0$ and $x = L_x/2$, in particular, has been assessed again by considering a homogeneous system in which pbc are applied to all directions. It has been verified that at high η the effect of interfaces is comparable in two and in three dimensions.

Dimensionality is a crucial parameter in the physics of critical states. For this reason the comparison of properties for 3D hard spheres and hard spheres plus an attractive tail has been carried out in full analogy with the 2D case, following again the critical isotherm. The definition of the potential model is the trivial extension of the 2D case (1), and the same $\delta = \sigma/2$ has been used in the two cases. The critical properties of the model are determined and discussed in Ref. [46]. According to this reference, the critical point of the model occurs at $\eta^* = 0.157 \pm 0.01$ and $T^*/\epsilon = 1.219 \pm 0.008$. Our samples differ from those used in Ref. [46] because they comprise a larger number of particles, and because they are limited by two parallel interfaces. Due to these differences, the sample at exactly the critical parameters of Ref. [46] appears to be divided in two slightly different phases. To make sure that the sample is homogeneous, the temperature of the simulation has been changed slightly to $T/\epsilon = 1.25$. At this temperature, the MC results still display large density fluctuations at η close to η^* that persist over long times apparently because of critical slowing down.

The results for the average length $\langle l \rangle$ of paths transmitted through the suspension of the square well particle is shown in Fig. 15, compared with the results of the 3D hard sphere model. The trend is the same as the 2D case, i.e., close to criticality $\langle l \rangle$ is lower for the hard sphere plus attractive tail model than for hard sphere samples, but the quantitative difference between the two sets of results is somewhat smaller in three dimensions, consistent with the generally accepted statement that the effects of criticality are stronger in two than in three dimensions. Also in this 3D case, the average length of reflected beams is longer for particles with the attractive tail than for pure hard spheres.

E. Amplification and output power distribution

In random lasers based on suspensions of colloidal particles, scattering and diffusion of light underlie the amplification of the input beam through stimulated emission

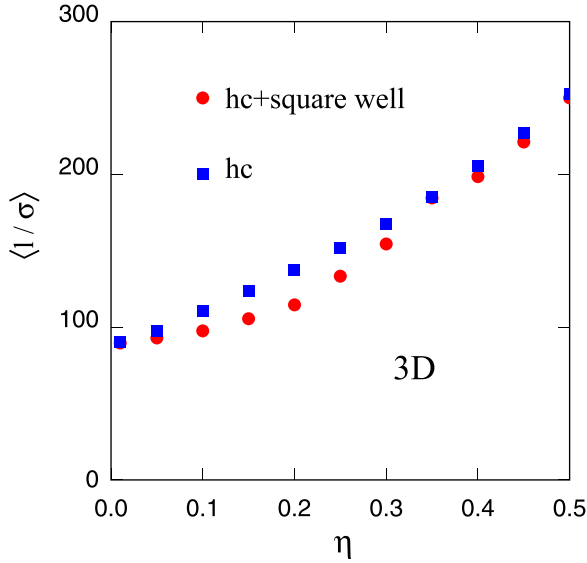


FIG. 15. Average length $\langle l \rangle$ of transmitted paths as a function of η . Blue filled squares: hs potential; red dots: hs plus attractive square well tail.

in the solution. Since the model discussed in the previous sections contains no details on the optical properties of the medium, the discussion of lasing properties is limited to statistical considerations on the length of transmitted paths and on the intensity of the emitted rays.

Each transmitted ray of initial intensity $i_0 \equiv I_{\text{inp}}$ (ideally, entering the slab as a single photon) will leave the slab after covering a distance l in its diffusive drift, emerging with an output intensity $I_{\text{out}} = i_0 \exp(\beta l)$, where β is the gain per unit length due to stimulated emission (see Sec. II). The overall amplification factor k_{ampl} therefore will be

$$k_{\text{ampl}} = \left\langle \frac{I_{\text{out}}}{I_{\text{inp}}} \right\rangle = \frac{\sum_{i \in T} \exp(\beta l_i)}{N_T + N_R}, \quad (18)$$

where $\sum_{i \in T}$ indicates the sum over the set of transmitted rays, while N_T and N_R are the number of transmitted and reflected rays, respectively. Provided $\beta(l)$ is small, k_{ampl} can be approximated as

$$k_{\text{ampl}} \approx T \exp(\beta \langle l \rangle) \quad (19)$$

[as anticipated in Eq. (11)] where T is the transmission coefficient and $\langle l \rangle$ is the average of the individual transmitted path lengths $\{l_i\}$. More precisely, because of the inequality of arithmetic and geometric means [64], the relation between the two expressions for k_{ampl} is in fact an inequality

$$k_{\text{ampl}} = \frac{I_{\text{out}}}{I_{\text{inp}}} = \frac{\sum_{i \in T} \exp(\beta l_i)}{N_T + N_R} > T \exp(\beta \langle l \rangle) \quad (20)$$

that becomes an equality in the limit of vanishing $\beta \langle l \rangle$: For this reason, $T \exp(\beta \langle l \rangle) > 1$ is a sufficient condition for amplification. Using the simulation data for T , it is possible to determine for each η the minimum β that provides amplification. The results are shown in Fig. 16 for 2D and in Fig. S9 of Ref. [53] for 3D, and represent the computational analog of the threshold dependence on dye molecules and scatterer concentration highlighted in experiments [65]. It might be

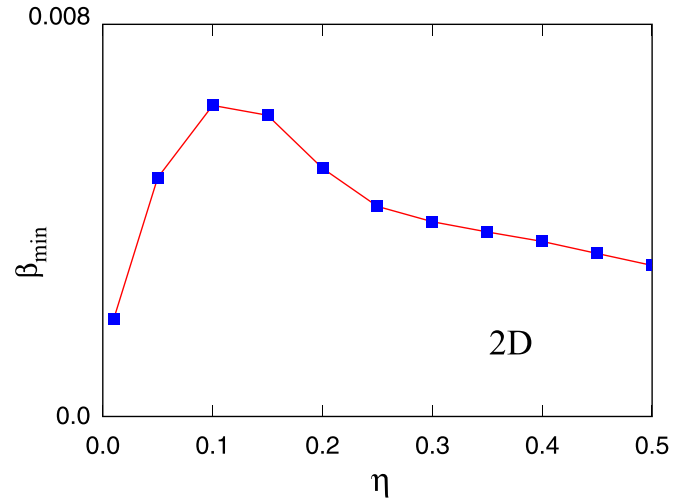


FIG. 16. Blue filled squares: Minimum value of the gain per unit length β required to achieve amplification $k_{\text{ampl}} > 1$. The line is a guide for the eye.

useful to point out that the results strictly depend on the size of the slab. It is precisely because of the ambiguous comparison of size in two and three dimensions that the results for the two different dimensionalities have not been reported on the same plot. The results show that the optimal range is at low and at high density, while the medium density range is somewhat disfavored, since it requires larger values of β to achieve amplification.

Besides the overall amplification, which is of interest for lasing, an important issue concerns the statistics of the power output from the slab made of colloidal particles in an optically active medium. The probability distribution $P_{\text{out}}(I)$ of the ensemble of output intensities has peculiar properties in the limit of large I that have been extensively investigated for their conceptual and applied interest [59].

As already stated, in the simple picture underlying the present study, a fraction T of the incoming rays will exit the slab with an intensity I_i amplified by a factor that depends on the length l_i of their trajectory within the slab. Then the simulation data for the length of each transmitted ray allows the direct computation of the intensity distribution of the emitted rays. The result for the high-intensity range is reported in Fig. 17 for the 2D case with $\eta = 0.1$ and $\eta = 0.5$. The double logarithmic scale makes it apparent that the emitted intensity follows an inverse power-law behavior, whose exponent depends on the parameter β selected for estimating the amplification. The same behavior is observed in all simulated cases, in both 2D and 3D samples. In experiments, inverse power-law decay of P_{out} usually is associated with a Lévy distribution, but its observation is far less general than in simulation [33]. It is likely that the difference between simulation and experiment is due to the simplicity of the model, which neglects every feature related to the microscopic optical processes underlying stimulated emission. In any case the computational results depend on the β value, which is arbitrary.

Additional insight into this statistical mechanics aspect can be gained from the observation that in both two and three

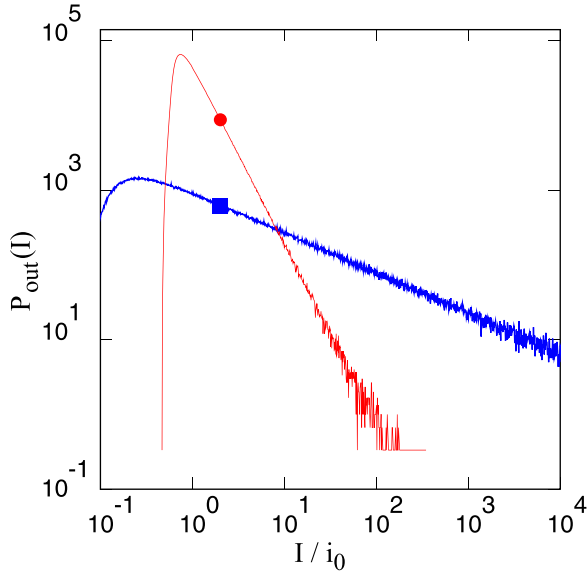


FIG. 17. Probability distribution of the output intensity I in two dimensions. Red curve (and dot): $\eta = 0.15$; blue curve (and filled square): $\eta = 0.5$. The output has been computed assuming the arbitrary value $\beta = 0.002$ as the amplification per unit length.

dimensions the Wald distribution gives a good fit of the smooth part $\bar{P}_T(I)$ of the distribution of transmitted path lengths, provided η is not too small. In the present model, a transmitted ray of initial intensity i_0 is emitted with a final intensity multiplied by $\exp(\beta l)$; therefore, the probability distribution $P_{out}(I)$ of emitted intensities I is fully determined by $P_T(I)$, since rays of intensity I are emitted by all paths whose length is

$$l(I) = \frac{\ln I}{\beta} - \ln(i_0), \tag{21}$$

which, at high I is approximated as $l(I) = \ln I/\beta$. However, the probability of paths having length $l \gg \langle l \rangle$ is $\bar{P}_T(I)$. Hence, using

$$P_{out}(I) = \bar{P}_T(l(I)) \frac{dl(I)}{dI} \tag{22}$$

one obtains

$$\begin{aligned} P_{out}(I) &= \frac{1}{I\beta} \sqrt{\frac{\lambda\beta^3}{2\pi(\ln I)^3}} \exp\left[-\frac{\lambda}{2\beta} \frac{(\ln I - \mu\beta)^2}{\mu^2 \ln I}\right] \\ &= \frac{1}{I\beta} \left(\frac{1}{I^{1/2}}\right)^{\frac{\lambda}{\beta\mu^2}} \sqrt{\frac{\lambda\beta^3}{2\pi(\ln I)^3}} \times C \times \exp\left[-\frac{\lambda\beta}{\ln I}\right], \end{aligned} \tag{23}$$

where $C = \exp(\lambda/\mu)$ is a constant.

In the limit of high-power I , the last exponential tends to 1. Neglecting the dependence of P_{out} on the logarithmic factor $(\ln I)^{-3/2}$ (whose derivative tends to zero in the limit of large I), the leading dependence on I is

$$P_{out}(I) \propto \frac{1}{I} \left(\frac{1}{I^{1/2}}\right)^{\frac{\lambda}{\beta\mu^2}}, \tag{24}$$

which has apparent similarities with the asymptotic behavior of the Lévy distribution. A precise equivalence requires *ad hoc* assumptions that are not inherent aspects of the model. Nevertheless, we observe that inserting into these expressions the values of μ and σ obtained from the fit, the β estimated for the lasing threshold (see Fig. 16), $\lambda/\beta\mu^2$ is close to one, and the exponent of I is close to $-3/2$. Even without any assumption, the inverse power behavior of $P_{out}(I)$ at large I represents a fat tail [59,66] that seems to be a characteristic feature of the power spectrum of random lasers. Previous studies have also attributed Lévy statistics to near-threshold conditions [67].

IV. DISCUSSION AND SUMMARY

The propagation of light in a random medium is a subject of great conceptual and practical interest, underlying, for instance, the development of random lasers and applications that range from speckle-free illumination and imaging [22], nanotechnology [68], and medical diagnostics [23]. Previous studies have investigated the statistical mechanics aspects of light propagation and amplification in random media using a variety of models of different sophistication. The most representative models, however, consist of random walks among scattering centers confined between two parallel surfaces located at $x = 0$ and $x = L_x$, leaving unconstrained the diffusion along the other directions [40]. In these models each step is determined by parameters drawn from preassigned probability distributions, deciding the length of the step (whose average is the mean-free path) as well as the change of propagation direction upon each scattering event. In virtually all cases these models, although sophisticated and useful, are generic (and thus also general), in the sense that they are not derived from a specific model of the distribution of scattering centers, and sometimes they do not quantitatively model a specific scattering mechanism. The novelty of the present approach is that it is tailored on a specific model of colloidal particles in a fluid. Correlations among particles are explicitly accounted for, and the effect of the interfaces or of different interparticle potentials or different thermodynamic conditions arises from the underlying model of particles and interfaces. Admittedly, the scattering mechanism implemented in the present model is simple, consisting of ideal reflection at the surface of the colloidal particles, and the wave character of light is neglected. These aspects, however, could be refined at least to some extent, especially in the direction of introducing different scattering mechanisms.

In this broad framework, two basic many-particle models have been investigated, consisting of purely repulsive hard-core particles and of similarly repulsive particles whose interaction potential, however, includes a square well attractive tail. Simulations have been carried out in two and three dimensions, although, for computational convenience and ease of visualization, more effort and emphasis have been devoted to the 2D case. The 2D case is not only a theoretical playground, since virtual 2D random lasers [69] have also been made.

Analysis of trajectories provides exact data for the propagation of light in the models that have been simulated.

Transmission and reflection coefficients have been computed as a function of packing fraction η in two and three dimensions, and approximated with a simple Padé form. The average length $\langle l \rangle$ of transmitted paths has been computed and found to display a massive increase at high η with respect to the minimum length corresponding to the width L_x of the slab. At $\eta = 0.5$, for instance, the average path exceeds the minimum path L_x by a factor 38 and 15 in two and three dimensions, respectively. More importantly, the probability distribution $P_T(l)$ of the length l of transmitted paths is broad, having high variance and excess kurtosis, corresponding to a sizable number of positive ($l > \langle l \rangle$) outliers. Given the exponential character of the amplification by the optically active medium, these outliers may have a disproportionate effect on the output power. At medium-high η , the Wald (also known as inverse Gaussian) distribution provides an accurate representation of $P_T(l)$ even in the long- l tail. Translating the analytical form of the Wald distribution into the power domain shows that the distribution of power intensity for the outgoing light follows an inverse power decay on the high-intensity range. Therefore, even the simple model that has been simulated has a characteristic output distribution characterized by the fat tail that has been extensively discussed for random lasers [70].

The distribution of scattering events (see Fig. 8) shows that, apart from interfacial effects that are sizable but localized, the intensity of light decreases linearly with increasing x , as a result of the diffusive propagation. Deviations are expected and observed at low η when the propagation of light is partly ballistic. This observation implies a Ohmic dependence of the transmission coefficient on the width of the slab, which has been verified by a single computation in two dimensions at $\eta = 0.300$ by doubling N as well as the width of the simulated slab.

Additional simulations have been performed on slightly modified models to investigate the effect of interfaces and of

weak polydispersivity on the system properties. More importantly, comparison between the results for the purely repulsive potential and for the case with a square well attractive tail shows that the important fluctuations around the critical state of the later model decrease the length of the transmitted paths and decrease the width of the $P_T(l)$ distribution, while the kurtosis is enhanced. This shows that the performance of random lasers based on colloidal particles can be tuned by changing the interaction among particles and the thermodynamic state of the system.

An example of complex property that can be investigated directly by a detailed and specific model is the loss of memory in the direction of rays in the diffusive regime of light propagation. Memory is rapidly lost, but on the short timescale it is sizable and peculiar, showing a predominant effect of backscattering. This property depends on the interplay of the scattering matrix of each reflection event with the correlation in the particles' position, and it is difficult to model *a priori*. In the present approach, it emerges automatically from the explicit description of correlations, including the effect of interfaces or of medium scale inhomogeneities.

In the future, the scattering matrix (here introduced only implicitly through the rules of geometric reflection) of different scattering mechanisms could be implemented, and the spatial correlation in the distribution of scattering centers could be modeled for different types of disordered media, providing quantitative data for specific materials and geometries. On the other hand, a simple modification of the experimental setup of Ref. [10], probing the systems with a laser beam narrower than the mm size of the particles, could closely reproduce the conditions of the computational model. Then comparison of the new results with those obtained using a broad, plane-wave-like illumination could disentangle the geometric aspects of the light propagation from the complexities of the scattering mechanism.

-
- [1] P. G. Hewitt, The physics of rainbows, *Sci. Teacher* **87**, 14 (2019).
 - [2] P. W. Milonni and J. H. Eberly, *Laser Physics* (John Wiley & Sons, Hoboken, NJ, 2010).
 - [3] R. V. Ambartsumyan, N. G. Basov, P. G. Kryukov, and V. S. Letokhov, A laser with a non-resonant feedback, *IEEE J. Quantum Electron.* **Qe-2**, 442 (1966).
 - [4] V. S. Letokhov, Generation of light by a scattering medium with negative resonance absorption, *Sov. Phys. JETP* **26**, 835 (1968).
 - [5] D. S. Wiersma, The physics and applications of random lasers, *Nat. Phys.* **4**, 359 (2008).
 - [6] H. Cao, Review on latest developments in random lasers with coherent feedback, *J. Phys. A: Math. Gen.* **38**, 10497 (2005).
 - [7] X. Meng, K. Fujita, S. Murai, and K. Tanaka, Coherent random lasers in weakly scattering polymer films containing silver nanoparticles, *Phys. Rev. A* **79**, 053817 (2009).
 - [8] F. R. Lamastra, R. De Angelis, A. Antonucci, D. Salvatori, P. Proposito, M. Casalboni, R. Congestri, S. Melino, and F. Nanni, Polymer composite random lasers based on diatom frustules as scatterers, *RSC Adv.* **4**, 61809 (2014).
 - [9] N. M. Lawandy, R. M. Balachandran, A. S. L. Gomes, and E. Sauvain, Laser action in strongly scattering media, *Nature (London)* **368**, 436 (1994).
 - [10] V. Folli, A. Puglisi, L. Leuzzi, and C. Conti, Shaken granular lasers, *Phys. Rev. Lett.* **108**, 248002 (2012).
 - [11] V. Folli, N. Ghofraniha, A. Puglisi, L. Leuzzi, and C. Conti, Time-resolved dynamics of granular matter by random laser emission, *Sci. Rep.* **3**, 2251 (2013).
 - [12] P. Sheng, *Introduction to Wave Scattering, Localization and Mesoscopic Phenomena* (Academic Press, San Diego, 1995).
 - [13] K. Vynck, R. Pierrat, R. Carminati, L. S. Froufe-Pérez, F. Scheffold, R. Sapienza, S. Vignolini, and J. J. Sáenz, Light in correlated disordered media, *Rev. Mod. Phys.* **95**, 045003 (2023).
 - [14] M. Segev, Y. Silberberg, and D. N. Christodoulides, Anderson localization of light, *Nat. Photon.* **7**, 197 (2013).
 - [15] P. W. Anderson, Absence of diffusion in certain random lattices, *Phys. Rev.* **109**, 1492 (1958).
 - [16] D. He, W. Cui, X. Liao, X. Xie, M. Mao, X. Sang, P. Zhai, Y. Zhao, Y. Huang, and W. Zhao, Electronic localization derived

- excellent stability of Li metal anode with ultrathin alloy, *Adv. Sci.* **9**, 2105656 (2022).
- [17] J. R. Franz, F. Brouers, and C. Holzhey, Theory of metal-non-metal transitions in liquid-metal alloys, *J. Phys. F: Met. Phys.* **10**, 235 (1980).
- [18] W. R. Mondal, N. S. Vidhyadhiraja, T. Berlijn, J. Moreno and M. Jarrell, Localization of phonons in mass-disordered alloys: A typical medium dynamical cluster approach, *Phys. Rev. B* **96**, 014203 (2017).
- [19] Y. Ma, W. Liu, Y. Cui, and X. Xiong, Multiple-scattering effects of atmosphere aerosols on light-transmission measurements, *Opt. Rev.* **24**, 590 (2017).
- [20] H. Gimperlein, S. Wessel, J. Schmiedmayer, and L. Santos, Ultracold atoms in optical lattices with random on-site interactions, *Phys. Rev. Lett.* **95**, 170401 (2005).
- [21] D. S. Wiersma, Disordered photonics, *Nat. Photon.* **7**, 188 (2013).
- [22] S. W. Chen, J. Y. Lu, B. Y. Hung, M. Chiesa, P. H. Tung, J. H. Lin, and T. C. Yang, Random lasers from photonic crystal wings of butterfly and moth for speckle-free imaging, *Opt. Express* **29**, 2065 (2021).
- [23] R. C. Polson and Z. V. Vardeny, Random lasing in human tissues, *Appl. Phys. Lett.* **85**, 1289 (2004).
- [24] N. Padiyakkuth, S. Thomas, R. Antoine, and N. Kalarikkal, Recent progress and prospects of random lasers using advanced materials, *Mater. Adv.* **3**, 6687 (2022).
- [25] E. P. Raposo and A. S. L. Gomes, Analytical solution for the Lévy-like steady-state distribution of intensities in random lasers, *Phys. Rev. A* **91**, 043827 (2015).
- [26] R. Pierrat and R. Carminati, Threshold of random lasers in the incoherent transport regime, *Phys. Rev. A* **76**, 023821 (2007).
- [27] X. Y. Jiang and C. M. Soukoulis, Time dependent theory for random lasers, *Phys. Rev. Lett.* **85**, 70 (2000).
- [28] P. Pradhan and N. Kumar, Localization of light in coherently amplifying random media, *Phys. Rev. B* **50**, 9644 (1994).
- [29] R. Frank, A. Lubatsch, and J. Kroha, Theory of strong localization effects of light in disordered loss or gain media, *Phys. Rev. B* **73**, 245107 (2006).
- [30] A. Lubatsch and R. Frank, Coherent transport and symmetry breaking-laser dynamics of constrained granular matter, *New J. Phys.* **16**, 083043 (2014).
- [31] A. Lubatsch and R. Frank, Self-consistent quantum field theory for the characterization of complex random media by short laser pulses, *Phys. Rev. Res.* **2**, 013324 (2020).
- [32] E. Ignesti, F. Tommasi, L. Fini, S. Lepri, V. Radhalakshmi, D. Wiersma, and S. Cavalieri, Experimental and theoretical investigation of statistical regimes in random laser emission, *Phys. Rev. A* **88**, 033820 (2013).
- [33] F. Tommasi, L. Fini, E. Ignesti, S. Lepri, F. Martelli, and S. Cavalieri, Statistical outliers in random laser emission, *Phys. Rev. A* **98**, 053816 (2018).
- [34] D. Sharma, H. Ramachandran, and N. Kumar, Gaussian-to-Lévy statistical crossover in a random amplifying medium: Monte Carlo simulation, *Opt. Commun.* **273**, 1 (2007).
- [35] A. Consoli and C. López, Decoupling gain and feedback in coherent random lasers: Experiments and simulations, *Sci. Rep.* **5**, 16848 (2015).
- [36] C. Conti, L. Angelani, and G. Ruocco, Light diffusion and localization in three-dimensional nonlinear disordered media, *Phys. Rev. A* **75**, 033812 (2007).
- [37] C. Goeuedard, D. Husson, C. Sauteret, F. Auzel, and A. Migus, Generation of spatially incoherent short pulses in laser-pumped neodymium stoichiometric crystals and powders, *J. Opt. Soc. Am. B* **10**, 2358 (1993).
- [38] H. Cao, Y. G. Zhao, S. T. Ho, E. W. Seelig, Q. H. Wang, and R. P. H. Chang, Random laser action in semiconductor powder, *Phys. Rev. Lett.* **82**, 2278 (1999).
- [39] X. Meng, K. Fujita, Y. Zong, S. Murai, and K. Tanaka, Random lasers with coherent feedback from highly transparent polymer films embedded with silver nanoparticles, *Appl. Phys. Lett.* **92**, 201112 (2008).
- [40] G. L. Rogers, Multiple path analysis of reflectance from turbid media, *J. Opt. Soc. Am. A* **25**, 2879 (2008).
- [41] I. M. Vellekoop and A. P. Mosk, Focusing coherent light through opaque strongly scattering media, *Opt. Lett.* **32**, 2309 (2007).
- [42] B. Philips-Invernizzi, D. Dupont, and C. Caze, Bibliographical review for reflectance and diffusive media, *Opt. Eng.* **40**, 1082 (2001).
- [43] C. H. Mak, Large-scale simulations of the two-dimensional melting of hard disks, *Phys. Rev. E* **73**, 065104(R) (2006).
- [44] S. C. Martin, B. B. Laird, R. Roth, and H. Hansen-Goos, Thermodynamics of the hard-disk fluid at a planar hard wall: Generalized scaled-particle theory and Monte Carlo simulation, *J. Chem. Phys.* **149**, 084701 (2018).
- [45] W. Rzyśko and A. Trokhymchuk, Vapor-liquid coexistence in 2D square-well fluid with variable range of attraction: Monte Carlo simulation study, *J. Chem. Phys.* **137**, 224505 (2012).
- [46] L. Vega, E. de Miguel, L. F. Ruil, G. Jackson, and I. A. McLure, Phase equilibria and critical behavior of square-well fluids of variable width by Gibbs ensemble Monte Carlo simulation, *J. Chem. Phys.* **96**, 2296 (1992).
- [47] O. E. Barndorff-Nielsen, T. Mikosch, and S. I. Resnick, *Lévy Processes: Theory and Applications* (Birkhäuser, Boston 2001).
- [48] J. W. Merrill, H. Cao, and E. R. Dufresne, Fluctuations and correlations of emission from random lasers, *Phys. Rev. A* **93**, 021801(R) (2016).
- [49] N. A. I. M. Kamil, W. I. Wan Zakiah, I. Ismail, S. R. Balakrishnan, M. Sahrim, J. Jamaludin, M. Othman, and S. Suhaimi Principles and characteristics of random lasers and their applications in medical, bioimaging and biosensing, *AIP Conf. Proc.* **2203**, 020017 (2020).
- [50] P. E. Wolf, G. Maret, E. Akkermans, and R. Maynard, Optical coherent backscattering by random media: An experimental study, *J. Phys. France* **49**, 63 (1988).
- [51] A. F. Ioffe and A. R. Regel, Non-crystalline, amorphous and liquid electronic semiconductors, in *Progress in Semiconductors*, Vol. 4, edited by A. F. Gibson (Heywood, London, 1960), pp. 237–291.
- [52] A. B. Davies and M. B. Mineev-Weinstein, Radiation propagation in random media: From positive to negative correlations in high-frequency fluctuations, *J. Quant. Spectrosc. Radiat. Transf.* **112**, 632 (2011).
- [53] See Supplemental Material at <http://link.aps.org/supplemental/10.1103/PhysRevE.109.014615> for the SM document reports: (i) the comparison of the length probability distribution given by simulation and by fitting with the Wald distribution; (ii) The probability distribution of exit angles of reflected rays in 2D; (iii) the comparison of light propagation properties in 2D

- hard disk samples, 2D hard disk plus attractive tail samples, 3D hard disk samples and 3D hard disk plus attractive tail samples.
- [54] L. F. Rojas-Ochoa, J. M. Mendez-Alcaraz, J. J. Sáenz, P. Scurtenberger, and F. Scheffold, Photonic properties of strongly correlated colloidal liquids, *Phys. Rev. Lett.* **93**, 073903 (2004).
- [55] J. S. Rowlinson and B. Widom, *Molecular Theory of Capillarity* (Oxford University Press, Oxford, 1982).
- [56] M. H. J. Hagen and D. Frenkel, Determination of phase diagrams for the hard-core attractive Yukawa system, *J. Chem. Phys.* **101**, 4093 (1994).
- [57] P. R. ten Wolde and D. Frenkel, Enhancement of protein crystal nucleation by critical density fluctuations, *Science* **277**, 1975 (1997).
- [58] C. Allain and M. Cloitre, Characterizing the lacunarity of random and deterministic fractal sets, *Phys. Rev. A* **44**, 3552 (1991).
- [59] P. Barthelemy, J. Bertolotti, and D. Wiersma, A Lévy flight for light, *Nature (London)* **453**, 495 (2008).
- [60] J. Bertolotti, K. Vynck, L. Pattelli, P. Barthelemy, S. Lepri, and D. S. Wiersma, Engineering disorder in superdiffusive Lévy glasses, *Adv. Funct. Mater.* **20**, 965 (2010).
- [61] M. Heinen, S. K. Schnyder, J. F. Brady, and H. Löwen, Classical liquids in fractal dimension, *Phys. Rev. Lett.* **115**, 097801 (2015).
- [62] A. Davis and A. Marshak, Lévy kinetics in slab geometry: Scaling of transmission probability, in *Fractal Frontiers*, edited by T. G. Dewey and M. M. Novak (World Scientific, Singapore, 1997), pp. 63–72.
- [63] E. Abrahams, P. W. Anderson, D. C. Licciardello, and T. V. Ramakrishnan, Scaling theory of localization: Absence of quantum diffusion in two dimensions, *Phys. Rev. Lett.* **42**, 673 (1979).
- [64] E. G. Kwon and K. H. Shon, On the arithmetic-geometric mean inequality, in *Finite or Infinite Dimensional Complex Analysis* (CRC Press, Boca Raton, FL, 2000).
- [65] J. Kitur, G. Zhu, M. Bahoura, and M. A. Noginov, Dependence of the random laser behavior on the concentrations of dye and scatterers, *J. Opt.* **12**, 024009 (2010).
- [66] C. Forbes, M. Evans, N. Hastings, and B. Peacock, *Statistical Distributions*, 4th ed. (John Wiley & Sons, Hoboken, NJ, 2011).
- [67] R. Uppu and S. Mujumdar, Dependence of the Gaussian-Lévy transition on the disorder strength in random lasers, *Phys. Rev. A* **87**, 013822 (2013).
- [68] H. Salama, B. Smaani, F. Nasri, and A. Tshipamba, Nanotechnology and quantum dot lasers, *J. Comput. Sci. Tech. Stud.* **5**, 45 (2023).
- [69] H.-W. Hu, G. Haider, Y.-M. Liao, P. Kumar Roy, R. Ravindranath, H.-T. Chang, C.-H. Lu, C.-Y. Tseng, T.-Y. Lin, W.-H. Shih *et al.*, Wrinkled 2D materials: A versatile platform for low-threshold stretchable random lasers, *Adv. Mater.* **29**, 1703549 (2017).
- [70] D. Sharma, H. Ramachandran, and N. Kumar, Lévy statistical fluctuations from a random amplifying medium, *Fluct. Noise Lett.* **6**, L95 (2006).